Late Neoarchean–Paleoproterozoic granitoid basement serves as an effective helium source rock in cratonic basins

Wenqi Li[a, b, c, d], Huichuan Liu[a, b, c, *], Greg Holland[e], Zheng Zhou[d], Jianfa Chen[a, b, c], Xiaoping Liu[a, b, c], Zhiqi Yu[a, b, c], Jian Li[f], Xiaobo Wang[f]

a. Hainan Institute of China University of Petroleum (Beijing), Sanya 572025, China

b. State Key Laboratory of Oil and Gas Resources and Exploration, China University of Petroleum (Beijing), Beijing 102249, China

c. College of Earth Sciences, China University of Petroleum (Beijing), Beijing 102249, China

d. Lancaster Environment Centre, Lancaster University, LA1 4YQ, UK

e. Department of Earth and Environmental Sciences, the University of Manchester, M13 9PL, UK

f. Research Institute of Petroleum Exploration and Development, Beijing 100011, China

Abstract:

The growing shortage of helium reserves presents a pressing worldwide concern. However, it remains ambiguous that how, when, and which type of tectonic environment the helium source rocks were formed. Recently, several helium-enriched gas fields have been discovered in the northern Ordos Block and confirmed to be crust-derived. Why late Neoarchean–Paleoproterozoic effective helium source rocks are distributed in the northern Ordos Block are still not clear. Detailed petrological, geochemical, geochronology, Sr-Nd isotopic and in-situ EPMA of U, Th-rich minerals studies were analyzed on the outcrops and drill cores of the basement of the northern Ordos Block to investigate the helium source rocks. The results show that (1) Late Neoarchean–Paleoproterozoic A-type granite and S-type granitoids are effective helium source rock types, and a large amount of U-Th rich accessory minerals (e.g., phosphate minerals, zircon, magnetite et al.) are preserved in alkaline feldspar and quartz. (2) The helium source rocks are classified into distinct temporal intervals: 2.60–2.45 Ga, 2.45–2.30 Ga and 1.95–1.80 Ga, respectively. The 2.60–2.45 Ga granitoids exhibit compositional signatures of I-type granites, consistent with magmatic arc tectonic settings linked to subduction zones. The 2.45–2.30 Ga granitoids display both A-type and I-type granitic affinities, indicating long live continental magmatic arc environment

* Corresponding author: lhc@cup.edu.cn

characteristics. The 1.95-1.80 Ga granitoids exhibit both A-type and S-type characteristics, suggesting formation in an extensional tectonic regime following continental collision. (3) The 2.60–2.45 Ga period is late Archean subduction-accretion and arc magmatism, followed by arc-continent collision; The 2.45–2.30 Ga period is a long-time arc-continental accretion process with multiple arc magmatism; The 1.95–1.80 Ga period represents continent-continent collision to post-collisional extension setting. Thus, the long-term arc-continental accretion and multistage crustal recycling of terrigenous sediments with high U and Th content, comparable to Phanerozoic subduction-accretionary orogens, explain why effective helium source rocks are enriched in the northern Ordos Block. By comparison of Khondalite Belt (NCC) with global Khondalite Belts, global Khondalite belts could be favorable areas for predicting the worldwide distribution of helium source rocks.

Key words: Helium source rocks, granitoids, tectonic environment, arc continent accretion, Cordilleran accretionary orogen

1 Introduction

Helium is one of noble gases with special properties: chemical inertness, low boiling point, and low density. It is integral to numerous advanced technologies, such as cryogenic superconductivity, aerospace, nuclear industry, and medical technology therefore helium is regarded as a crucial resource for modern industry (Cai et al., 2010; Chen, et al., 2021). Worldwide helium-rich reservoirs are predominantly concentrated in a limited number of countries, including the United States, Qatar, Algeria, and Russia, which are dominantly located in ancient cratons (Li et al., 2024). By contrast, China faces significant helium resource scarcity and remains in an exploratory phase, actively pursuing technological innovation to address this critical limitation. Helium reserves have been found in Ordos Block, Sichuan Basin and Tarim Basin (Dai et al., 2017; Liu et al., 2022; Ni et al., 2014; Peng et al., 2022; Tao et al., 2019; Zhang et al., 2019), with lower helium content than that of above helium-rich countries. In recent

years, several helium-rich gas fields have been discovered in the northern Ordos Block, including the Dongsheng gas field (Peng et al., 2022), Daniudi gas field (Liu et al., 2022) and Sulige gas field (Dai et al., 2017), with helium content exceeding industrial helium thresholds (He % > 0.05%). The majority of helium in petroleum gas, which predominantly consists of ^{4}He, is derived from the α-decay of ^{235}U, ^{238}U, and ^{232}Th within sedimentary strata, basement rocks, or the crust. (Ballentine and Burnard, 2002; Brown, 2010). Previous studies have come to an agreement that the helium within the natural gas in the northern Ordos Block originates from large-scale ancient granite and metamorphic basement rocks (Liu et al., 2022; Peng et al., 2022). The high helium concentrations detected in natural gas reservoirs of the northern Ordos Block correlate with anomalously high uranium and thorium abundances in the basement rocks, coupled with the prolonged accumulation of radiogenic decay reaction. In addition, significant progress has been achieved in uranium exploration within the lower Cretaceous strata of the northern Ordos Block, with the origin of the uranium deposit attributed to the weathering of the basement rocks (Akhtar et al., 2017; Chen et al., 2019; Zhang et al., 2017). The formation of sedimentary uranium deposits provides additional evidence that the basement rock in the northern basin is characterized by high uranium enrichment. Thus, during the enrichment accumulation of helium, it is initially released from the granitic basement. Subsequently, fault activities that connect the reservoir with the basement facilitate the transport of helium, which migrates into the overlying strata along these faults and accumulates alongside conventional hydrocarbon gases. Therefore, it can be inferred that it is the high U and Th contents of the basement rocks making them effective helium source rocks for the helium-rich gas fields.

However, the factors contributing to the extensive spatial distribution of helium source rocks in the northern Ordos Block are still not clear. Furthermore, it remains ambiguous that how and when and which type of tectonic environment the helium source rocks were formed. Located within the western block of the North China Craton

(NCC), the Ordos Block represents a classic example of a cratonic basin distinguished by its substantial basement thickness (Fig. S1). Currently it is generally accepted that the Western Block of the North China Craton (NCC) resulted from the convergence between the northern Yinshan Block and the southern Ordos Block, occurring along the Khondalite Belt approximately between 1.95 and 1.85 Ga (Li et al., 2011; Liu et al., 2019; Liu et al., 2021; Yin et al., 2014; Zhang et al., 2017; Zhao and Guo, 2012; Zhao et al., 2005), finally forming the basement of Ordos Block. In addition, the basement of the Ordos Block is extensively overlain by sedimentary strata, which significantly hinders the understanding and characterization of the basement.

Therefore, to investigate the helium source rocks, comprehensive analyses involving petrography, geochemistry, U–Pb geochronology, Sr–Nd isotope and in-situ EPMA of uranium- and thorium-rich minerals were conducted on surface outcrops and drill core samples collected from the Northern Ordos Block. Our study aims to answer which rock types in granitic basement are effective helium source rocks, when effective helium source rocks were formed, what source region effective helium source rocks belong to, and which tectonic environment helium source rock were formed. Our novel data provides important insights into understanding the rock types, ages, protoliths, source regions and tectonic environments of effective helium source rocks, which could account for the reason why effective helium source rocks are enriched in the Northern Ordos Block.

2 Geological setting

The Ordos Basin, an extensive hydrocarbon-rich basin situated upon the Ordos Block, features a broad basement structure covered by substantial sedimentary deposits. Occupying a major area of the Western Block of the North China Craton (NCC), the Ordos Block is delineated by prominent tectonic boundaries: it adjoins the Yinshan Block (YB) and Khondalite Belt to its northern margin, the Helanshan-Liupanshan Thrust Belt (H-LTB) to its western edge, the Qinling Orogenic Belt (QB) to its southern

boundary, and the Trans-North China Orogen (TNCO) along its eastern flank (Figs. S1 and S2).

The Ordos Block represents a tectonically stable cratonic segment of the North China Craton (NCC), displaying limited deformation and seismic activity. It is distinguished by substantial crustal thickness, averaging around 41.4 km, low geothermal gradients, and pronounced high-velocity seismic anomalies (Wang et al., 2014). Structurally, the block exhibits a characteristic two-tiered arrangement, consisting of a crystalline basement of Precambrian beneath sedimentary sequences deposited from the Mesoproterozoic through the Phanerozoic, which collectively reach thicknesses of roughly 10 km (Kusky and Mooney, 2015).

Current geological outcrop studies indicate that the Khondalite Belt, extending nearly 1,000 kilometers, is exposed along the Jining-Daqingshan-Wulashan-Qianlishan-Helan Mountains, located between the northern margin of the Ordos Block and the Yinshan Block (Zhao et al., 2001, 2005, 2013). The Khondalite Belt is composed of graphite-garnet-sillimanite-K-feldspar gneiss, felsic paragneiss, quartzite, marble, and minor amphibolite (Lu et al., 1996). The protolith sedimentation occurred after 2.0 Ga (Yin et al., 2011; Dan et al., 2012), and the belt subsequently underwent granulite facies metamorphism followed by retrograde metamorphism during the period of 1.95 to 1.83 Ga (Guo et al., 2012; Jiao et al., 2015; Jiao et al., 2013; Santosh et al., 2009; Santosh et al., 2007; Wan et al., 2013b; Yin et al., 2011; Yin et al., 2009). Concurrently, S-type granitic magmatism occurred synchronously with the metamorphism (Jiao et al., 2013; Peng et al., 2012; Yin et al., 2011; Yin et al., 2009). Metamorphic supracrustal rocks and metamorphic plutonic intrusions are exposed in Jining and Wulashan-Daqingshan region, including the Neoarchean Sanggan Group (or Xinghe Group), the Neoarchean-Paleoproterozoic Wulashan Group, and the late Paleoproterozoic Meidaizhao Group. Chronological studies reveal that the northern margin of Ordos Block records multiple phases of magmatic activity, including granitoids at 2.55–2.45 Ga, 2.30–2.0 Ga, 1.96–1.94 Ga, and 1.85–1.82 Ga, as well as

mafic rocks at 2.55–2.50 Ga, 2.45–2.37 Ga, 2.06 Ga, 1.97–1.92 Ga, and 1.84 Ga. These magmatic events were accompanied by metamorphic events at ~2.5 Ga, 2.45–2.40 Ga, and 1.95–1.85 Ga (Santosh et al., 2007, 2009; Dong et al., 2013, 2014; Wan et al., 2013; Liu et al., 2014c, 2017; Zhong et al., 2014). This indicates that the northern Ordos Block experienced multiple geological events during the late Neoarchean to the Paleoproterozoic.

Analysis of drill core samples obtained from several exploration wells within the northern part of the Ordos Block indicates that the regional basement predominantly comprises Neoarchean granitoid gneisses as well as Paleoproterozoic paragneisses subjected to amphibolite- to granulite-facies metamorphic conditions, accompanied by subordinate granitoid gneiss (Zhang et al., 2021). Core samples from the basement reveal granitic magmatic activities at ~2.5 Ga and ~2.0 Ga, which are consistent with the granitic magmatic events recorded at 2.55–2.45 Ga and 2.30–2.0 Ga in the Khondalite Belt distribution area along the northern margin of the Ordos Block (Tian et al., 2023; Wan et al., 2013a; Zhang et al., 2015; Zhang et al., 2021). Zircon and monazite U-Pb dating also identifies two distinct sets of metamorphic ages at 1.96–1.94 Ga and 1.9–1.88 Ga (Hu et al., 2013; Wan et al., 2013; Wang et al., 2014, 2019; Zhang et al., 2015; Gou et al., 2016; He et al., 2016), which correspond to the two sets of metamorphic ages documented in the Khondalite series of the Wulashan-Daqingshan and Helan Mountains areas along the northern margin at ~1.95 Ga and ~1.87 Ga (Yin et al., 2011; Cai et al., 2013). The comparable lithological assemblages and consistent magmatic-metamorphic histories observed across both regions provide compelling evidence that the basement rocks in the northern Ordos Block can be directly correlated with the geological domain of the Khondalite Belt. Both regions exhibit a ~2.5 Ga granitic basement overlain by high-grade metamorphic supracrustal rocks and underwent magmatic activities during the middle to late Paleoproterozoic (2.30–2.0 Ga) and metamorphic modifications at 1.95–1.85 Ga. These findings demonstrate that the basement in the northern Ordos Block predominantly consists of Neoarchean to

Paleoproterozoic supracrustal metamorphic rocks and granitic gneisses, which experienced repeated episodes of magmatism and metamorphism spanning the Neoarchean through the Paleoproterozoic eras.

Numerous substantial gas fields have been identified within the Upper Paleozoic tight sandstone reservoirs of the Ordos Block (Liu et al., 2009; Dai, 2016). Among these, the Dongsheng and Daniudi gas fields are distinguished by notably elevated helium concentrations (He et al., 2022; Liu et al., 2022; Peng et al., 2022). In the gas field of north Ordos Block, the Upper Paleozoic strata are developed from bottom to top as the Taiyuan Formation (C_3t), Shanxi Formation (P_1s), Lower Shihezi Formation (P_1x), Upper Shihezi Formation (P_2sh), and Shiqianfeng Formation (P_3s). In the Dongsheng Gas Field, the main source rocks for Upper Paleozoic natural gas are represented by coal-bearing strata within the Taiyuan and Shanxi Formations, consisting primarily of coal seams, carbonaceous mudstones, and dark mudstones (He et al., 2022). Highly quality reservoirs are represented by the conglomeratic coarse sandstones and coarse-grained sandstone layers found within the Lower Shihezi and Shanxi Formations (He et al., 2022). Moreover, the substantial and widespread occurrences of mudstone and silty mudstone within the Upper Shihezi and Shiqianfeng Formations serve as highly effective regional sealing strata. The main gas producing layer is the Shihezi Formation and Taiyuan Formation of Permian strata (Peng et al., 2022).

3. Results

3.1 Petrographic characteristics

A total of eight granitoid gneiss samples were obtained from the Daqingshan-Ulashan area, with their lithological characteristics and ages presented in Table 1 and illustrated in Figs. 1 and 2

Table 1 The lithologies and age of the granitoids samples from the Daqingshan Complex

Sample	Rock Type	Major Mineral Composition	Accessory Minerals	Age (Ma)
BT-1-3-a	Medium- to coarse-grained charnockitic gneiss	Quartz (25%-35%), Perthite (45%-60%), Plagioclase (5%-10%), Hypersthene (5%), minor biotite	Monazite, Zircon, Magnetite	2319 ± 25
BT-2-a	Granodioritic gneiss	Plagioclase (25%-30%), Biotite (15%), Quartz (15%-20%), Amphibole (10%-15%)	Monazite, Zircon, Magnetite, Apatite, Rutile, Titanite	2307.3 ± 8.6
BT-3-a	Granitic gneiss	Potassium feldspar (25%-30%), Plagioclase (20%-25%), Quartz (10%-15%), Biotite, Amphibole	Monazite, Zircon, Apatite	2551 ± 14
BT-4-b	Biotite-bearing monzogranitic gneiss	Plagioclase (20%-30%), Potassium feldspar (15%-25%), Quartz (15%), Biotite (10%), Amphibole	Monazite, Zircon, Magnetite	2578 ± 19
BT-6-b	Medium- to coarse-grained charnockitic gneiss	Hypersthene, Perthite (25%-35%), Plagioclase (15%-25%), Quartz (20%-30%), minor biotite (<5%)	Zircon, Apatite, Ilmenite	2475 ± 21
BT-7-b	Monzogranitic gneiss	Plagioclase (20%-30%), Potassium feldspar (15%-25%), Quartz (15%), Biotite (5%-10%), Amphibole	Monazite, Zircon, Apatite, Magnetite	2307 ± 30
BT-10-a	Monzogranitic gneiss	Plagioclase (25%-30%), Potassium feldspar (20%-30%), Quartz (15%), Biotite (10%), Amphibole (10%)	Zircon, Titanite, Monazite	1883 ± 27
BT-14-a	Monzogranitic gneiss	Plagioclase (20%-25%), Potassium feldspar (20%-25%), Quartz (15%-20%), Biotite (5%-10%), Amphibole (10%)	Zircon, Magnetite, Monazite	1834 ± 16

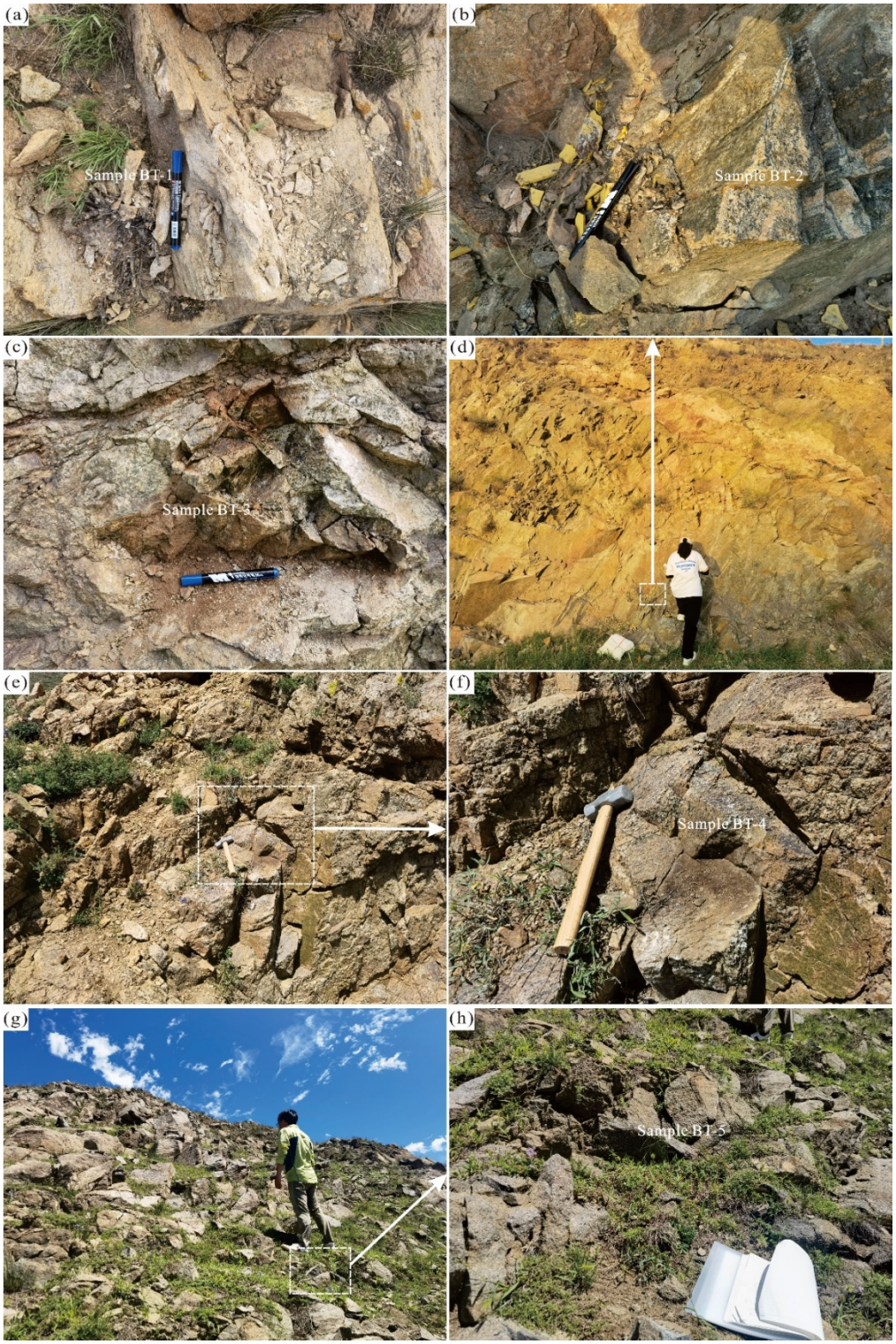

Fig. 1. The Photographs of outcrops of the late Neoarchean - Paleoproterozoic granitoid samples collected from the KB. BT-1-3a: Charnockitic gneiss; BT-2-a: Granodioritic gneiss; BT-3-b: Granitic gneiss; BT-4-a: Biotite-bearing monzogranitic gneiss; BT-6-b: Charnockitic gneiss; BT-7-b: Monzogranitic gneiss; BT-10-a: Monzogranitic gneiss; BT-14-f: Monzogranitic gneiss

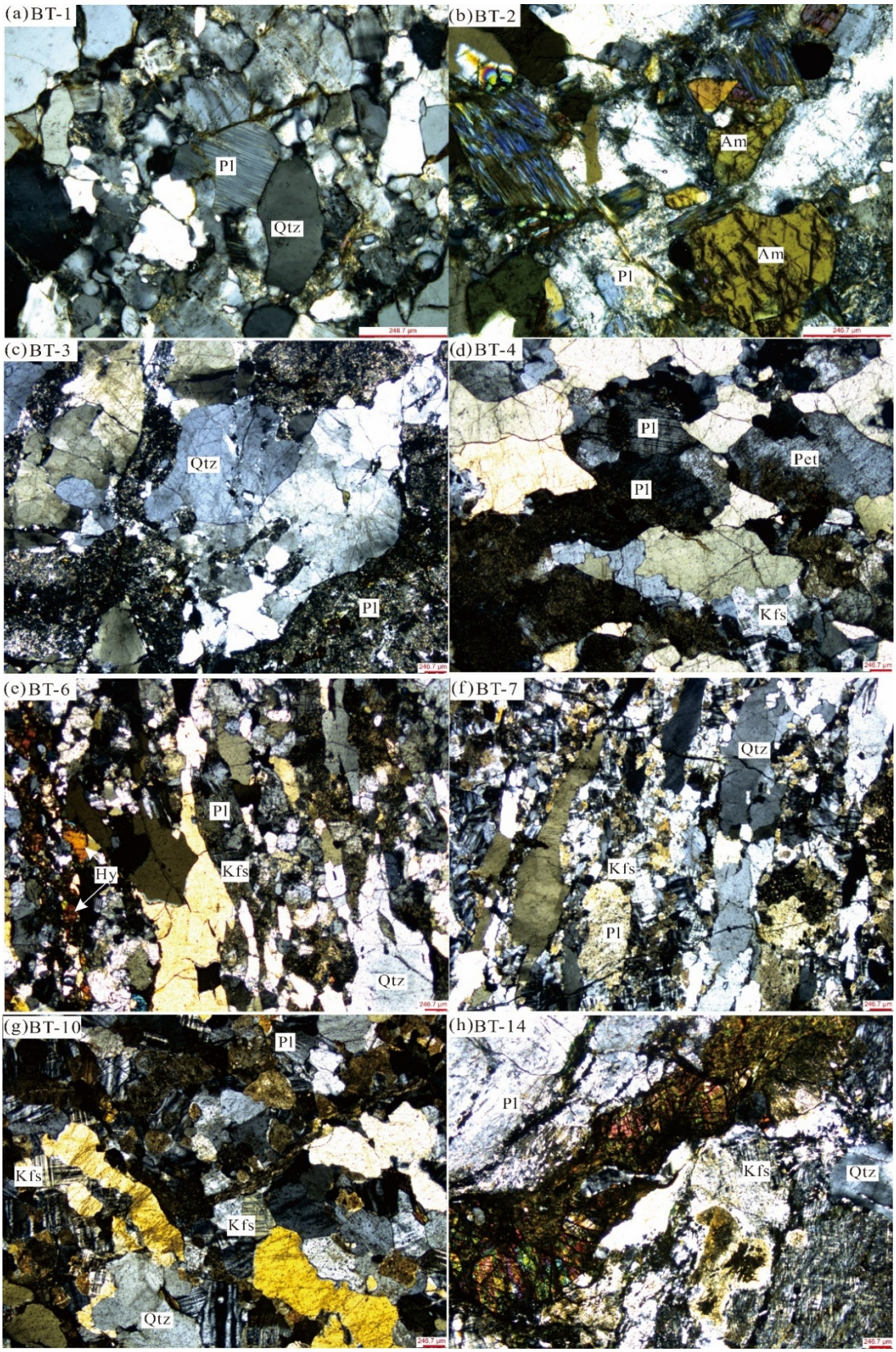

Fig. 2. Photomicrographs of granitoids samples. BT-1-3a: Charnockitic gneiss; BT-2-a: Granodioritic gneiss; BT-3-b: Granitic gneiss; BT-4-a: Biotite-bearing monzogranitic gneiss; BT-6-b: Charnockitic gneiss; BT-7-b: Monzogranitic gneiss; BT-10-a: Monzogranitic gneiss; BT-14-f: Monzogranitic gneiss.

3.2. Zircon U–Pb ages

The zircon U–Pb dating results for granitoid gneisses from the Daqingshan–Ulashan region are summarized in Table S1 and graphically presented in Figs. 3, 4 and 5. Cathodoluminescence (CL) imaging reveals that zircon grains from these samples commonly exhibit distinct magmatic oscillatory zoning patterns, and their Th/U ratios vary between 0.08 and 2.83, indicative of a magmatic genesis. Sample BT-1-3 (charnockitic gneiss) yields a crystallization age of 2319 ± 25 Ma, while BT-2-b shows two distinct phases: a core age of 2307 ± 9 Ma and overgrowth rim age of 1880 ± 21 Ma, indicating late magmatic reactivation. Older Neoarchean ages are recorded in BT-3-b (2551 ± 14 Ma) and BT-4-b (2578 ± 19 Ma). Younger Paleoproterozoic events are evident in BT-6-b (2475 ± 21 Ma cores and 1898 ± 21 Ma rims), BT-7-b (2307 ± 30 Ma cores and 1945 ± 13 Ma rims), BT-10-a (1883 ± 27 Ma), and BT-14-f (1834 ± 16 Ma). The data suggest prolonged crustal evolution involving Archean basement formation (2.60–2.45 Ga) followed by Paleoproterozoic magmatic pulses (2.45–2.30 Ga), with evidence of metamorphic overprinting in some samples (e.g., BT-4-b showing potential high-grade metamorphic resetting). Zircon morphologies (100–250 μm lengths, aspect ratios 1:1–1:4) and internal structures correlate with discrete magmatic episodes documented in Figs. 5 and 6.

3.3 Major- and trace-element geochemistry

The major and trace element geochemical data are provided in Table S2. Sample BT-3, BT-4 and BT-6 of 2.60–2.45 Ga display magnesian to ferroan signatures, with low- to high-potassium affinities. Geochemically, they range from calcic to calc-alkalic in nature and exhibit metaluminous to slightly peraluminous characteristics. These samples are marked by a pronounced enrichment in light rare earth elements (LREE) and relative depletion in heavy rare earth elements (HREE), along with distinct positive europium (Eu) anomalies. Additionally, they show depletion in high-field-strength

231 elements such as niobium (Nb) and tantalum (Ta), coupled with significant enrichment
232 in large-ion lithophile elements including barium (Ba), potassium (K), rubidium (Rb),
233 and strontium (Sr). Samples BT-1, BT-2, and BT-7, approximately 2.30 Ga, exhibit
234 magnesian compositions with low- to high-potassium contents, ranging from alkalic to
235 calc-alkalic affinities. They display metaluminous to slightly peraluminous
236 geochemical signatures. These samples are enriched in light rare earth elements (LREE)
237 and depleted in heavy rare earth elements (HREE), with either positive or negative
238 europium (Eu) anomalies. Furthermore, they are characterized by depletion in high-
239 field-strength elements such as niobium (Nb) and tantalum (Ta), and significant
240 enrichment in large-ion lithophile elements including barium (Ba), potassium (K),
241 rubidium (Rb), and strontium (Sr). Samples BT-10 and BT-14, dated between 1.95 and
242 1.80 Ga, are characterized by ferroan compositions with high potassium contents,
243 displaying alkalic to calc-alkalic affinities and metaluminous to mildly peraluminous
244 signatures. Geochemically, they are enriched in light rare earth elements (LREE) and
245 depleted in heavy rare earth elements (HREE), with subtle europium (Eu) anomalies.
246 Additionally, they show depletion in high-field-strength elements such as niobium (Nb)
247 and tantalum (Ta), along with notable enrichment in large-ion lithophile elements
248 including barium (Ba), potassium (K), rubidium (Rb), and strontium (Sr).

249 **3.4 In-situ Hf isotopic compositions in Zircon**

250 The in-situ hafnium (Hf) isotopic compositions of zircon grains from the granitoid
251 samples are provided in Table S3. The zircons $\varepsilon_{Hf}(t)$ values from the samples of 2.60–
252 2.45 Ga is between +2.0 and +7.4. The average depleted mantle model ages (T_{DM2}) of
253 the crustal source span from 2878 to 2526 Ma, with the majority of values clustering
254 between 2.8 and 2.6 Ga. Zircons from the 2.30 Ga samples yield $\varepsilon_{Hf}(t)$ values ranging
255 between –2.8 and +1.4. Corresponding depleted mantle model ages (T_{DM2}) fall within
256 the range of 3025 to 2771 Ma, suggesting derivation from an older crustal source.
257 Zircon $\varepsilon_{Hf}(t)$ values from the 1.95–1.80 Ga samples range from –8.9 to –0.2, indicating

significant crustal reworking. The corresponding depleted mantle model ages (T_{DM2}) span from 3036 to 2542 Ma, reflecting contributions from ancient crustal components.

3.5 Whole rock Sr-Nd isotope compositions

The whole-rock Sr–Nd isotopic data are summarized in Table S4. For samples dated between 2.60 and 2.45 Ga, ($^{87}Sr/^{86}Sr$)i ratios range from 0.700641 to 0.701996, while $\varepsilon_{Nd}(t)$ values vary from +0.98 to +2.30. Corresponding T_{DM1} model ages span from 2770 to 2507 Ma, and T_{DM2} model ages range from 2878 to 2526 Ma. Samples from the 2.30 Ga group exhibit ($^{87}Sr/^{86}Sr$)i ratios between 0.697138 and 0.702981, with $\varepsilon_{Nd}(t)$ values ranging from –2.00 to +1.46. The T_{DM1} ages fall within 2758 to 2592 Ma, and T_{DM2} ages between 3025 and 2771 Ma. For the 1.90–1.80 Ga samples, initial 8($^{87}Sr/^{86}Sr$)i ratios vary from 0.701549 to 0.706241, and $\varepsilon_{Nd}(t)$ values span a broader range from –4.47 to +3.78. The corresponding T_{DM1} ages lie between 2573 and 2290 Ma, while T_{DM2} ages range from 3036 to 2542 Ma.

Fig. 3. Cathodoluminescence images of representative zircons from four granitoids (BT-1-3, BT-2, BT-3 and BT-4) from Ulashan-Daqingshan region. Red circles and blue circles mark the locations of U-Pb ages and Lu-Hf isotopic, respectively, with ages and $\varepsilon_{Hf}(t)$ values shown near the zircons.

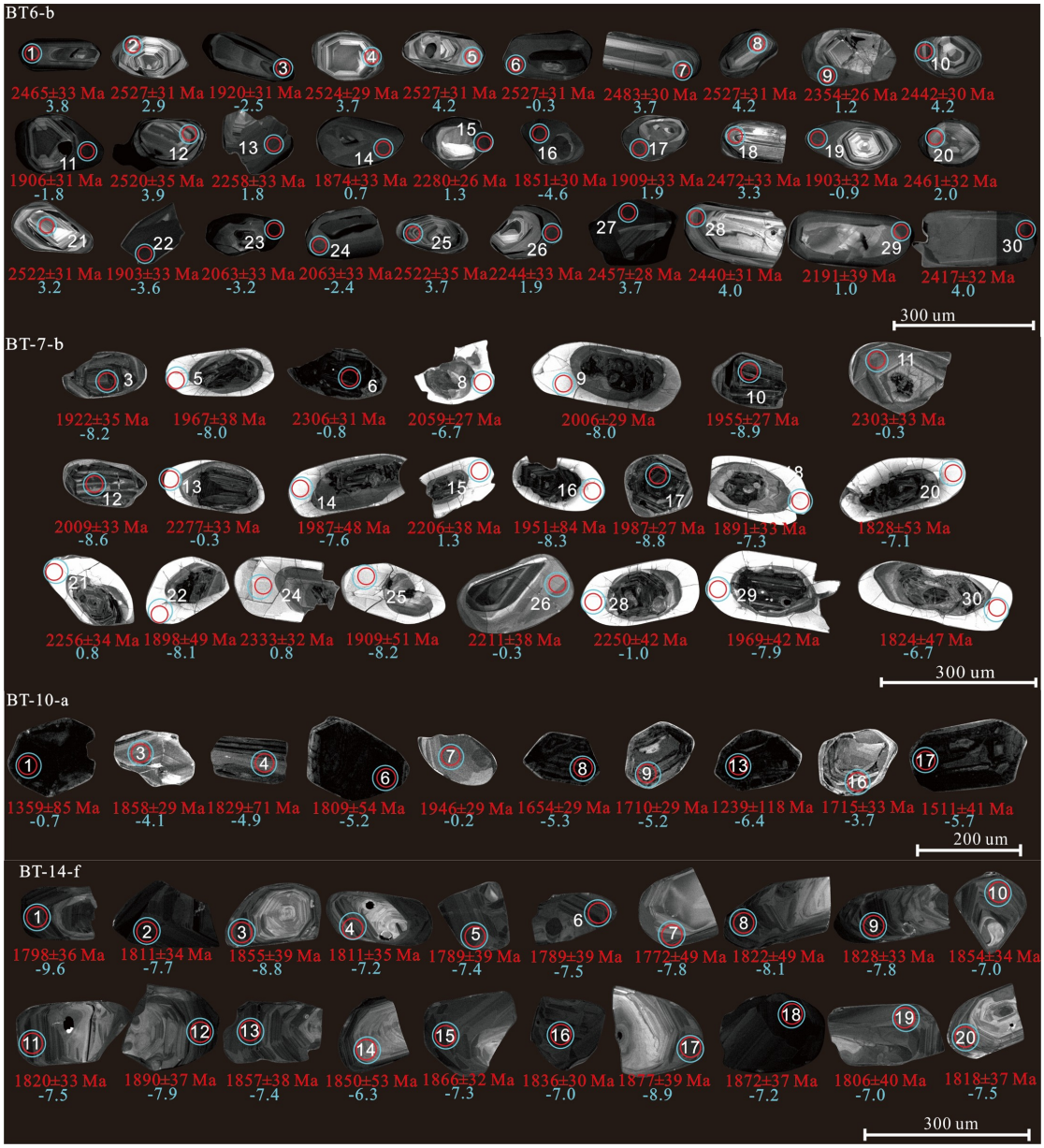

Fig. 4. Cathodoluminescence images of representative zircons from four our granitoids (BT-6, BT-7, BT-10 and BT-14) from Ulashan-Daqingshan region. Red circles and blue circles mark the locations of U-Pb ages and Lu-Hf isotopic, respectively, with ages and $\varepsilon_{Hf}(t)$ values shown near the zircons.

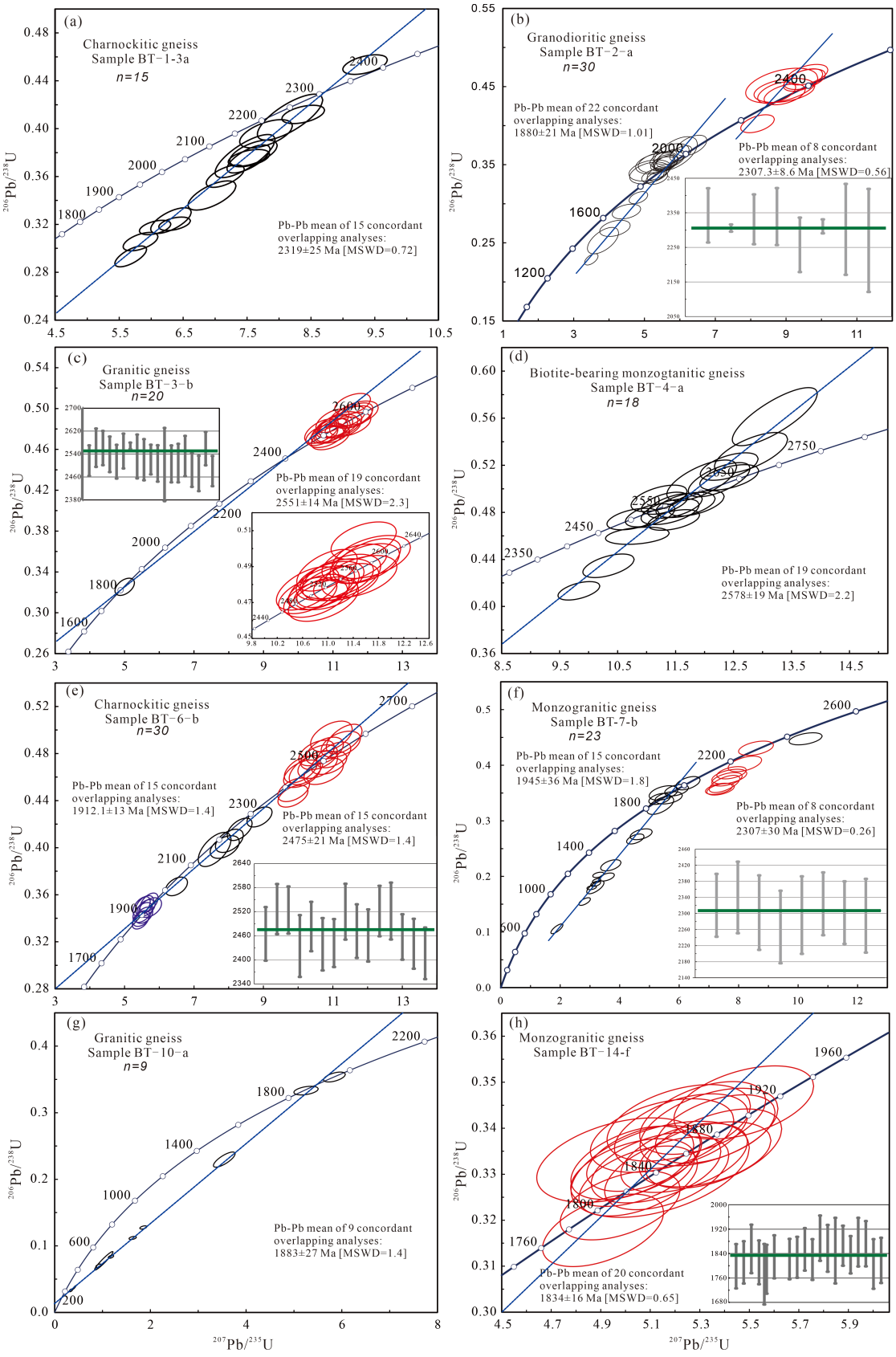

Fig. 5. Zircon U-Pb Concordia diagram of granitoids samples from the Daqingshan Complex

3.6 EPMA analysis

The major element compositions of U- and Th-rich minerals are provided in Table S5. Energy-dispersive spectroscopic analysis identified a suite of U- and Th-bearing accessory minerals, including monazite, thorite, zircon, apatite, magnetite, xenotime, rutile, and titanite. These minerals, which are predominantly accessory minerals, are widely distributed across the analyzed samples. Their grain sizes typically range from 10 μm to 200 μm, with the exception of one elongated grain measuring approximately 600 μm. Due to extensive isomorphic substitution within these accessory phases, precise mineral identification is often hindered. Consequently, tentative classification through electron probe microanalysis (EPMA) was conducted based on dominant elemental compositions in cases where mineral identity remained ambiguous (Table S5). As shown in Figs. 7 and 8, uranium and thorium are primarily hosted within monazite, apatite, xenotime, magnetite, and zircon. These U- and Th-rich phases are either embedded within magmatic minerals—such as K-feldspar, albite, and quartz—or located along the interfaces between them.

4. Discussion

4.1. Effective helium source rock

The concept of "helium source rock" was initially proposed by Burwash and Cumming (1974) and subsequently cited by Brown (2010). Drawing a parallel with the definition of hydrocarbon source rocks, helium source rocks are described as “a *type of rock enriched in uranium (U) and thorium (Th) capable of generating and releasing significant quantities of helium*” (Zhang et al., 2020). Analogous to the role of organic matter in assessing hydrocarbon source rocks, the concentrations of uranium (U) and thorium (Th) serve as the primary criteria for determining whether a given rock type qualifies as a helium source rock. As noted by Brown (2010), uranium and thorium

311 concentrations are significantly higher in granite and shale compared to those in
312 sandstone and limestone. Extensive studies by various researchers on helium source
313 rocks associated with helium-rich gas fields worldwide have identified that granitoid,
314 organic-rich shale and bauxite rock are potential helium source rocks (Ballentine and
315 Sherwood Lollar, 2002; Broadhead, 2005; Gold and Held, 1987; Johnson, 2012;
316 Nikonov, 1973; Pierce et al., 1964; Ruedemann and Oles, 1929; Zhang et al., 2020). As
317 for helium-rich gas fields in Ordos Block, granitic basement, organic-rich shale and
318 bauxite rock are thought to be potential helium source rocks (Li et al., 2022; Liu et al.,
319 2022; Peng et al., 2022; Wang et al., 2023a). As the volume scale of granitic basement
320 is much larger than that of organic-rich shale and bauxite rock, we prefer granitic
321 basement rocks to be the helium source in Ordos Block.

322 Our samples consist of three types granitoids of the basement including: I-type
323 granitoids, A-type granitoids and S-type granitoids (Detailed discussion in 5.2). A-type
324 and S-type granitoids generally exhibit higher concentrations of uranium (U) and
325 thorium (Th) compared to I-type granites, indicating their greater potential as helium
326 source rocks (Fig. 6a). Furthermore, S-type granites typically contain uranium (U) and
327 thorium (Th) concentrations that exceed those of both A-type and I-type granites by
328 approximately an order of magnitude, underscoring their elevated potential as helium
329 source rocks (Fig. 6a). Given the limited dataset obtained from our collected samples,
330 a comprehensive review of existing granitoid data from the basement of the Northern
331 Ordos Block was conducted. The comparison reveals that our results align well with
332 the broader statistical dataset, supporting the reliability and representativeness of our
333 findings.

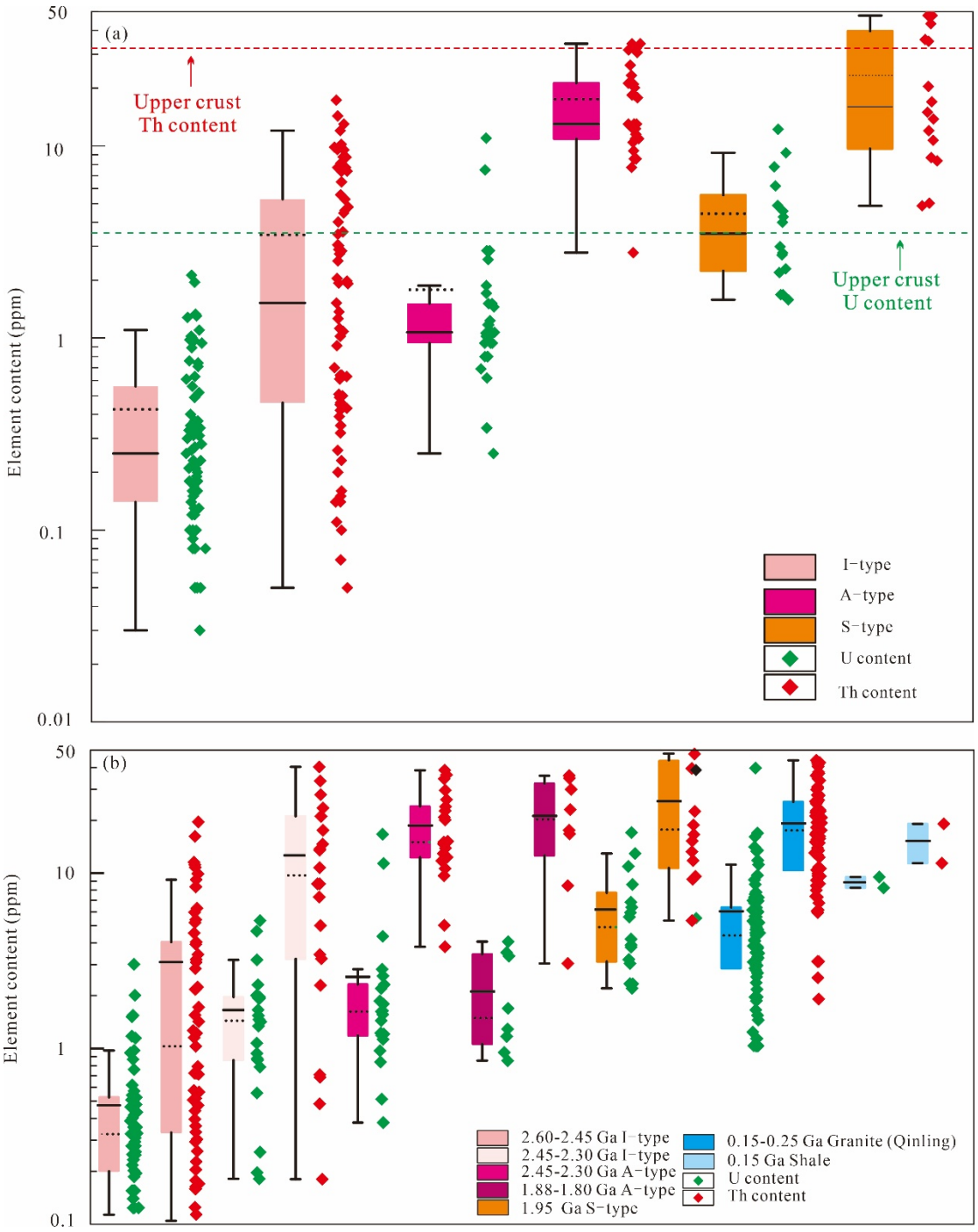

Fig. 6. (a) The current U and Th content in the three types granitoids of the basement in the northern Ordos Block. (b) The initial U and Th content of the granitoids of the basement in the Northern Ordos Block. Data source: 2.60–2.45 Ga I-type granitoids (Dong et al., 2023; Liu et al., 2017; Wang et al., 2021) and this study; 2.45–2.30 Ga I-type granitoids (Wang et al., 2021) and this study; 2.46-2.45 Ga A-type granitoids (Ouyang et al., 2020); 2.45–2.30 Ga A-type granitoids (Ouyang et al., 2020; Wang et al., 2022a) and this study; 1.88–1.80 Ga A-type granitoids (Wang et al., 2022b) and

this study; 1.87 Ga S-type granitoids (Dan et al., 2014; Zhang et al., 2016); 0.15-0.25 Ga granites from Qinling (Zhang et al., 2020); Shale layer from Dongsheng gas field (Wang et al., 2023a).

In addition, utilizing the present-day concentrations of uranium (U) and thorium (Th), we estimated the initial U and Th contents of the granitoid rocks located along the northern margin of the Ordos Block. In comparison with the younger granitic rocks from the Qinling Mountains along the southern margin of the Ordos Block and the shale-type hydrogen source rocks in the Dongsheng Gas Field, the granitoids located on the northern margin of the Ordos Block demonstrate superior potential as helium source rocks. This is attributed to their higher uranium and thorium concentrations, greater geological age, and substantial volumetric presence (Fig. 6b).

Table 2. Type and distributions of U and Th rich minerals in granitoids

Minerals	U content(wt.%)	Th content(wt.%)	Occurrence frequency	EPMA times
monazite	0.0058-1.5854 (0.6378)	1.7635-16.7191 (5.3230)	very high	155
thorite	0.3351-0.9359	51.8930-52.7371	rare	2
zircon	0-0.6415 (0.1136)	0-1.4728 (0.0820)	high	97
apatite	0.0067-0.1649 (0.0605)	0.0018-0.0738 (0.0274)	high	64
magnetite	0.0032-0.1378 (0.0052)	0.0017-0.0799 (0.0198)	high	64
titanite	0.0135-0.3233 (0.1128)	0.0141-0.0990 (0.0487)	medium	19
xenotime	0.2050-1.0150 (0.4959)	0.0013-0.1072 (0.5081)	medium	15
rutile	0.0063-0.0983 (0.0520)	0.0008-0.0438 (0.0172)	medium	22
ilmenite	0.0064-0.0798 (0.0411)	0.0042-0.2423 (0.0676)	medium	15

As discussed in section 5.1, 2.45–2.30 Ga A-type granitoids and I-type granitoids and 1.95–1.80 Ga A-type granitoids and S-type granitoids are believed to be effective helium source rock type in the north Ordos Block. 2.60–2.45 Ga I-type granitoids exhibit the lowest U and Th content among the three types granitoids. In terms of U and Th content, 2.60–2.45 Ga I-type granitoids seem not to be effective helium source rock. However, 2.60–2.45 Ga I-type granitoids correspond to the 2.50 Ga crust growth event, exhibiting the largest rock volume of upper continental crust. Thus, 2.60–2.45 Ga I-type granitoids are supposed to be good helium source rock.

From the rock scale to mineral scale, our observations indicate that uranium (U) and thorium (Th) are primarily concentrated within accessory mineral phases. Through

EMPA, we identified U and Th-rich minerals including monazite, thorite, zircon, apatite, magnetite, titanite, xenotime, rutile and ilmenite (Fig. 7). Among the U and Th-rich accessory minerals, phosphate minerals (monazite and xenotime) exhibit the highest U and Th and high frequency. Other minerals, including zircon, magnetite, titanite, rutile and ilmenite exhibit lower U and Th content and medium frequency. It is noteworthy that U- and Th-bearing accessory minerals are commonly hosted within, or occur at the boundaries between, primary magmatic phases such as K-feldspar, albite, and quartz (Fig. 8). Moreover, these U- and Th-rich minerals frequently exhibit close spatial association with alkaline feldspar, as illustrated in Fig. 8.

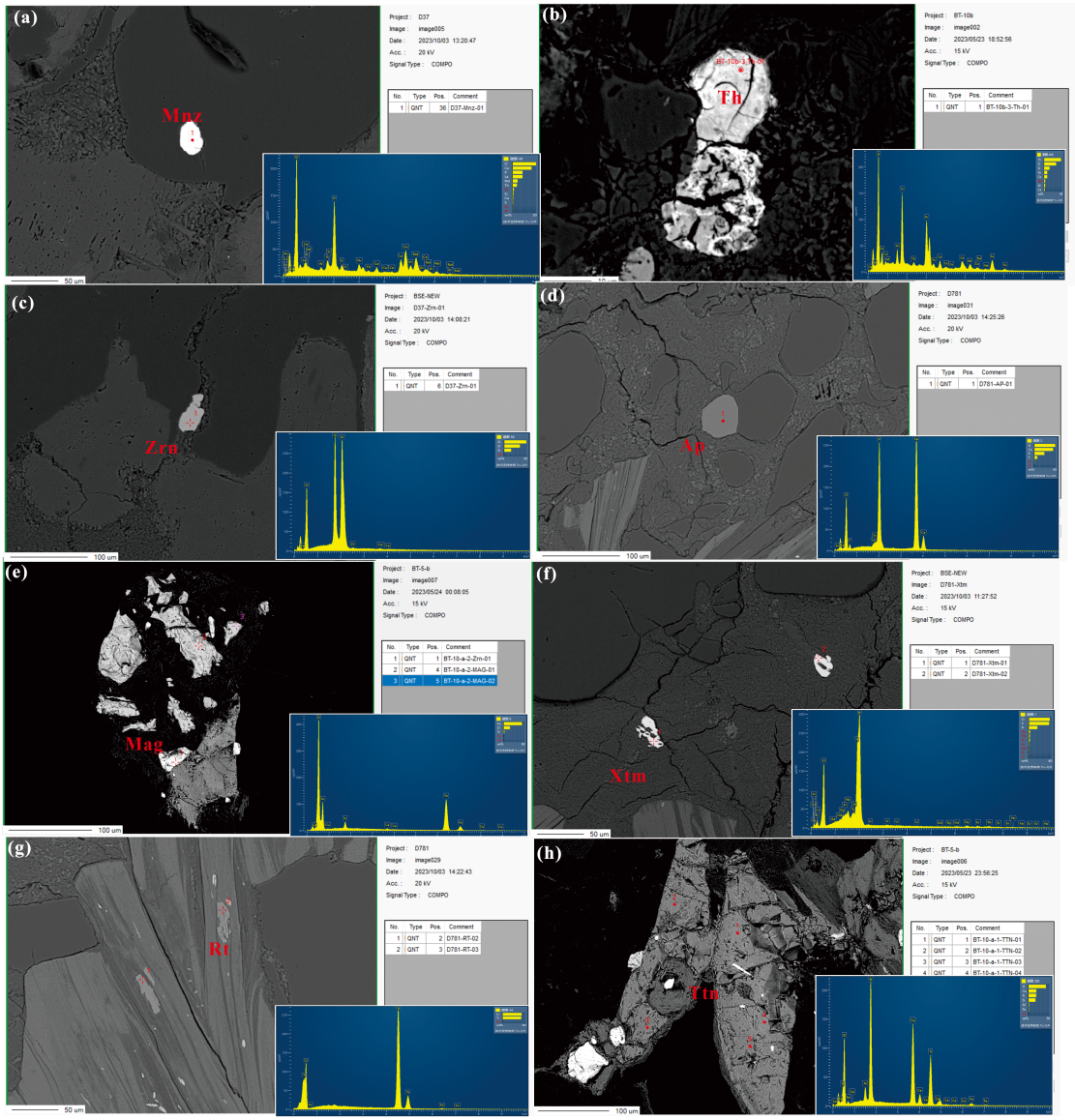

Fig. 7. Backscattered electron images identifying U, Th rich minerals within the granitoids samples.

U- and Th-bearing minerals include monazite (a), thorite (b), zircon (c), apatite (d), Magnetite (e), xenotime (f), magnetite, rutile (g) and titanite (h). Abbreviations: Mnz: Monazite; Xtm: Xenotime; Ap: Apatite; Mag: Magnetite; Zrn: Zircon; Rutile: Rt. Titanite: Ttn.

The generation of crust-derived helium (^{4}He) is calculated based on the radioactive decay formula, which has been described detailly in (Halford et al., 2022). According to the geological history of late Neoarchean–Paleoproterozoic period, the proportion is assumed as A-type (10%), S-type (10%), and I-type (80%) granitoids. ^{4}He production from different helium source units is shown in Table 3. Despite accounting for only 10% by volume, S-type granitoids contribute the largest share (46.4%) due to high U/Th concentrations. By contrast, although I-type granitoids exhibit lower U/Th concentrations, its 80% volume proportion results in a substantial contribution (43.5%). The result also shows that basement granitoids generate 3–4 orders of magnitude more helium than that of shale layer and bauxite layer.

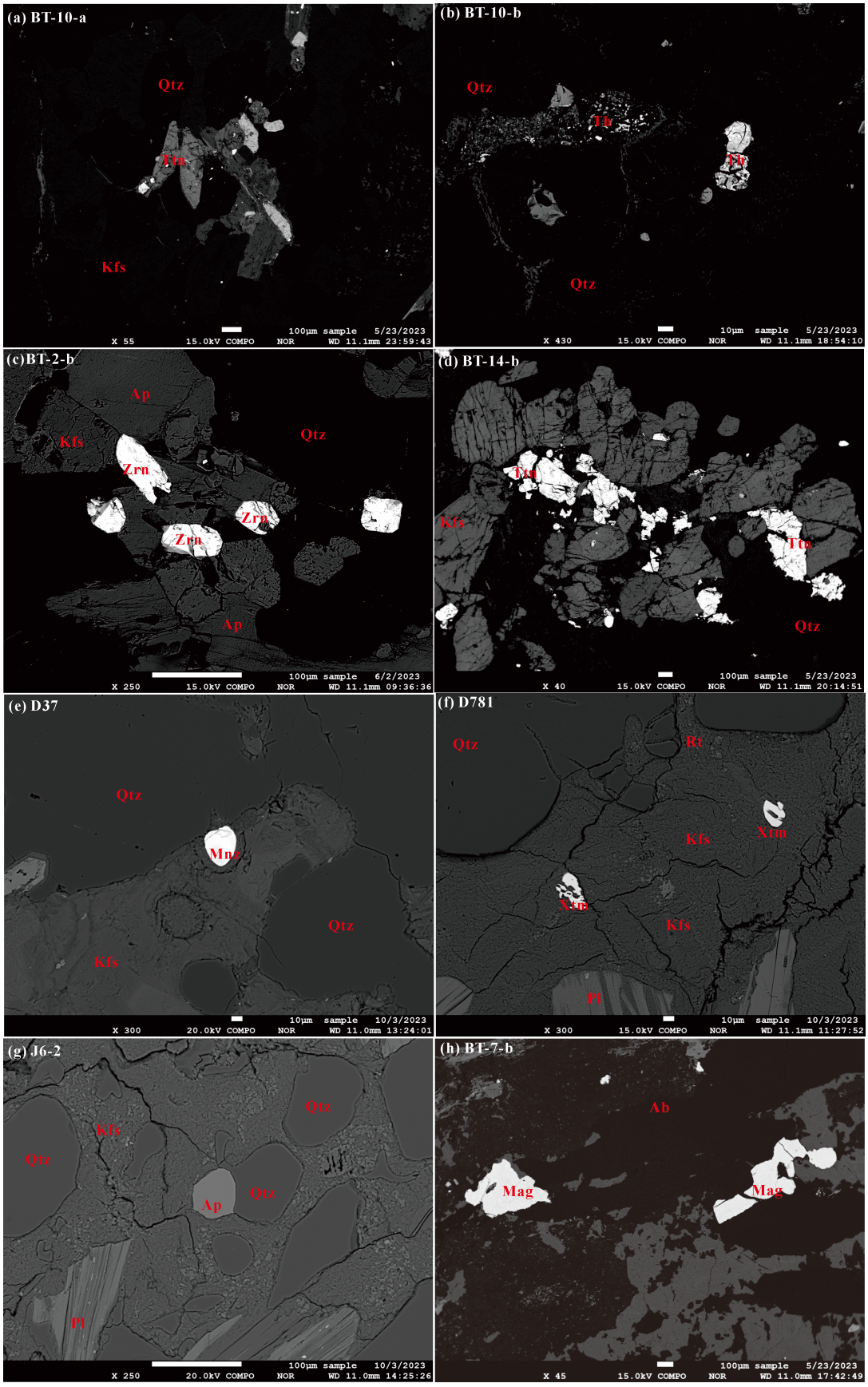

387

388 Fig. 8. Representative BSE (backscattered electron) images of U, Th rich minerals within the

389 granitoids samples from the Daqingshan Complex. Abbreviations: Mnz: Monazite; Xtm:

Xenotime; Ap: Apatite; Mag: Magnetite; Zrn: Zircon; Rutile: Rt. Titanite: Ttn.

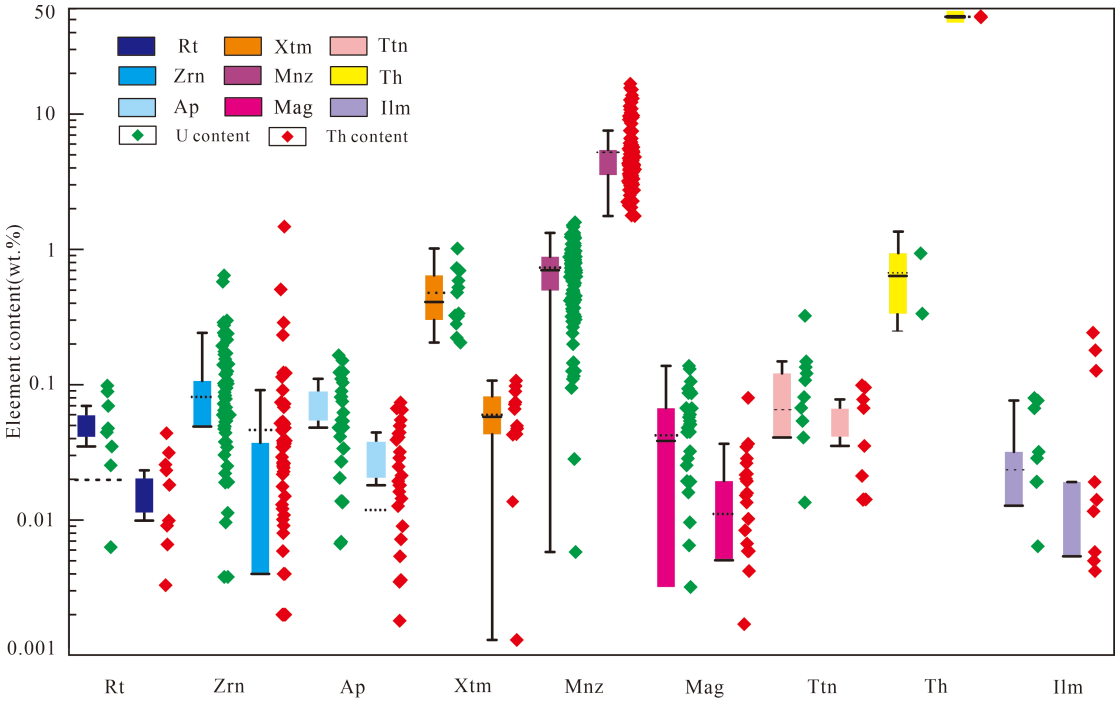

Fig. 9. The U and Th contents in U- and Th-rich minerals in the granitoids of the basement in the Northern Ordos Block

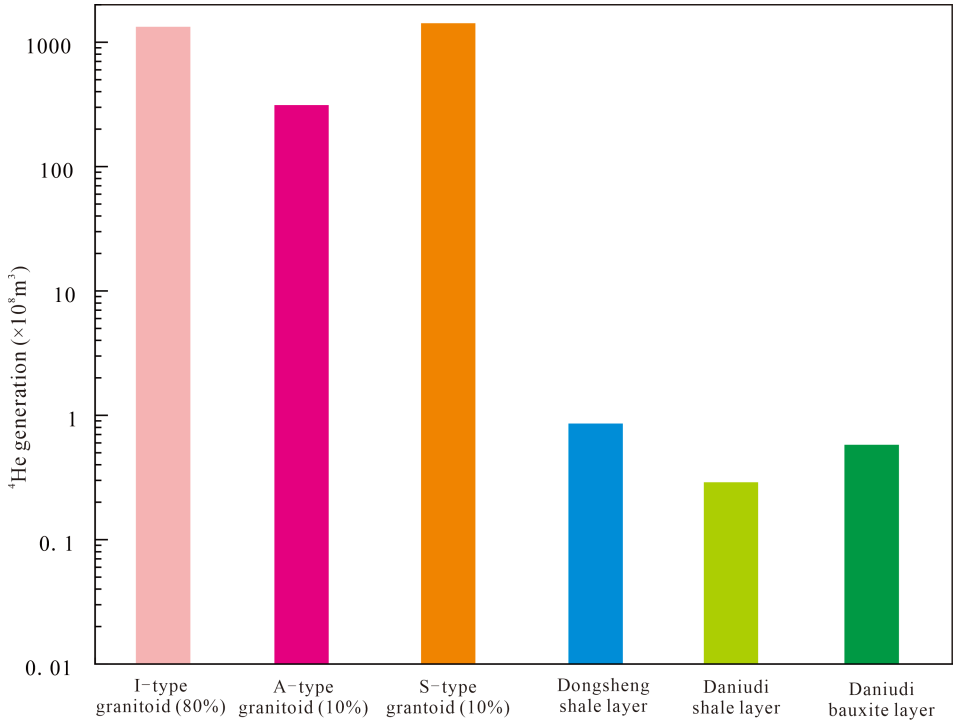

Fig. 10. ^{4}He production from different helium source units in the northern Ordos Block. Data from (Dai et al., 2012; Gao et al., 2023; Ji et al., 2013; Liu et al., 2012; Liu et al., 2015)

Table 3 ^{4}He production from different helium source units in the northern Ordos Block

Parameter	Proportion	U	Th	Age	Area	Thickness	Density	Porosity	Weighted Contribution
Unit	%	ppm	ppm	Ma	km^2	km	g/cm^3	%	m^3
A-type Granitoid	10%	1.78	17.3	2000	50,000	5	2.65	2.62	3.12×10^{10}
S-type Granite	10%	4.44	23.31	2000	50,000	5	2.65	2.62	1.42×10^{11}
I-type Granite	80%	0.31	2.73	2000	50,000	5	2.65	2.62	1.33×10^{11}
Total	100%	—	—	—	—	—	—	—	3.06×10^{11}
Dongsheng shale layer	—	5.61	13.09	270	10,000	0.02	1.5	6.6	0.86×10^{8}
Dongsheng bauxite layer	—	—	—	300	10,000	0.002	2.5	6.6	—
Daniudi shale layer	—	4	19	270	2,000	0.03	1.5	6.6	0.29×10^{8}
Daniudi bauxite layer	—	20.35	57	300	2,000	0.012	2.5	6.6	0.58×10^{8}

4.2. Sources and petrogenesis of helium source rock

The 2.60–2.45 Ga granitoids are geochemically characterized by elevated concentrations of SiO_2, Na_2O, and Al_2O_3, enrichment in potassium, and trends consistent with calc-alkalic magmatic evolution (Fig. 11). These granitoids fall within the magnesian to ferroan field, display low- to high-K affinities, and range from calcic to alkali-calcic in nature. They are also classified as metaluminous to slightly peraluminous. A notable feature of these granitoids is their high strontium (Sr) content, with most samples exceeding 400 ppm, and comparatively low concentrations of yttrium (Y) and ytterbium (Yb), averaging 10.55 ppm and 0.96 ppm, respectively. Additionally, they are enriched in rare earth elements, particularly light rare earth elements (LREE), while showing depletion in heavy rare earth elements (HREE), as illustrated in Fig. 12a. Elevated Sr/Y and $(La/Yb)_N$ ratios further support their

classification as part of the tonalite-trondhjemite-granodiorite (TTG) suite (Fig. 12a, b). Trace element data indicate enrichment in large-ion lithophile elements (LILE) such as K, Rb, and Ba, and depletion in high-field-strength elements (HFSE) including Nb, Ta, U, and Ti (Fig. 12a, b). On trace-element discrimination diagrams, most samples plot within the volcanic-arc granite field (Fig. 15f), consistent with formation in a subduction-related magmatic arc setting. The overall geochemical signature aligns with that of Cordilleran I-type granitoids, as described by Frost et al. (2001), supporting a tectonic origin linked to subduction processes.

I-type granitoids may originate through two primary mechanisms: (1) fractional crystallization of mantle-derived basaltic magma (Barth et al., 1995) or (2) partial melting of sub-alkaline meta-basalts followed by subsequent fractional crystallization (Rapp and Watson, 1995). Regarding the 2.60–2.45 Ga granitoids in the Ulashan–Daqingshan region, zircon $\varepsilon_{Hf}(t)$ values for all analyzed samples are uniformly positive, as illustrated in Figs. 11 and 12. The corresponding depleted mantle two-stage Hf model ages (T_{DM2}) are predominantly clustered between 2.7 and 3.0 Ga (Fig. 14b), suggesting that these granitoids were derived from juvenile crustal material that originally separated from the mantle during the period ca. 2.87–2.56 Ga. These interpretations are consistent with the findings reported by Liu et al. (2017), Wang et al. (2021), and Dong et al. (2023), further supporting the hypothesis that the Ulashan–Daqingshan granitoids were generated from juvenile crustal sources formed during the late Archean.

The granitoid samples dated to 2.30 Ga and 1.88–1.80 Ga display elevated concentrations of SiO_2, Na_2O, and Al_2O_3, along with notable potassium enrichment and exhibit calc-alkalic magmatic differentiation trends. Geochemically, these rocks are classified as magnesian, with low- to high-K contents, and range from calcic to alkali-calcic in nature. They also fall within the metaluminous to slightly peraluminous granitoid category (Fig. 11). According to prior research, subalkaline to peralkaline granites enriched in highly charged cations, such as Zr, Nb, Y, and REE, are typically associated with A-type granite signatures (Whalen et al., 1987; Eby, 1992). The whole-

rock geochemical data of these samples are consistent with this classification, as evidenced by their positions on discrimination diagrams (Figs. 20 and 21), thereby supporting their interpretation as A-type granitoids (Altherr et al., 2000; Bonin, 2007; Eby, 1992; Frost and Frost, 2011; Whalen et al., 1987).

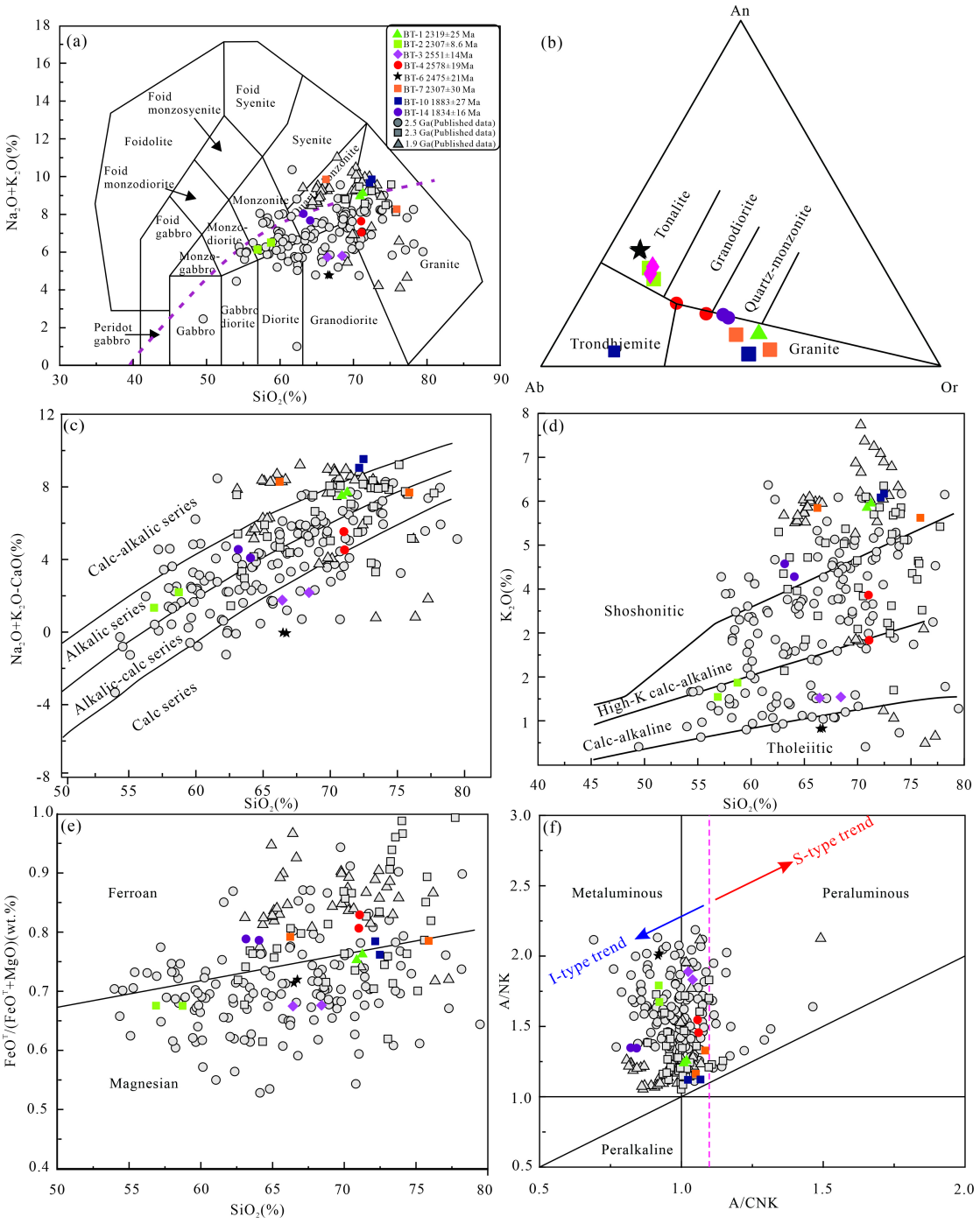

Fig. 11. Geochemical classification of granitoids samples from the Daqingshan Complex. (a): Total alkali vs silica diagram (Middlemost, 1994). (b) An-Ab-Or diagram (after Barker, 1979); (d): K_2O vs. SiO_2 diagram (Rollinson, 1993). (c): $Na_2O + K_2O$ - CaO vs SiO_2 diagram (after Frost et al.,

2001). (d): K_2O vs. SiO_2 diagram (Rollinson, 1993). (e) Plot of $FeO^T/(FeO^T+MgO)$ vs SiO_2 (Frost et al., 2001). (f): A/NK [$Al_2O_3/(Na_2O + K_2O)$] vs. A/CNK [$Al_2O_3/(CaO + Na_2O + K_2O)$] (after Maniar & Piccoli, 1989). Data sources: ca. 2.6–2.45 Ga (Ma et al., 2013a; Ma et al., 2013b; Ma and Zhong, 2018; Ouyang and Guo, 2020; Ouyang et al., 2020; Tian et al., 2023; Wang et al., 2023b; Zhang et al., 2011; Zhang et al., 2012; Zhang et al., 2023; Zhang et al., 2014), ca. 2.45–2.2 Ga (Dan et al., 2012; Wang et al., 2020; Wang et al., 2022a) , ca. 2.2–2.0 Ga (Wang et al., 2022c; Xu et al., 2020).

The origin of A-type granites has been a subject of extensive debate, with three primary genetic models proposed: (1)Partial melting (PM) model suggests that A-type granites form through the partial melting of diverse crustal sources (Collins et al., 1982; Frost et al., 1999; Frost and Ronald Frost, 1997; Whalen et al., 1987); (2) fractional crystallization (FC) model of mantle-derived alkaline basalts (Loiselle, 1979; Turner et al., 1992; Vander Auwera et al., 2003). (3) The assimilation-fractional crystallization (AFC) model indicates the contamination of mantle-derived alkaline basalts by Archean crustal material in the middle to upper crust (Li et al., 2019). Additionally, the mixing of more than two end-member lithologies can produce hybrid magmas (Eby, 1992; Mingram et al., 2000; Taylor and McLennan, 1995). The zircon Hf isotopic data reveal $\varepsilon_{Hf}(t)$ values ranging from –2.8 to +1.5, with corresponding depleted mantle model ages (T_{DM2}) between 3.02 and 2.77 Ga (Figs. 11 and 12), indicating that these granitoids were generated through the partial melting of ancient crustal sources. Similarly, the Hf isotopic signatures and T_{DM2} ages of the ~2.30 Ga granitoids support their derivation from the partial melting of older continental crust. For the 1.88–1.80 Ga granitoids, zircon $\varepsilon_{Hf}(t)$ values range from -8.9 to -0.2, and T_{DM2} model ages span from 3.03 to 2.54 Ga. These values further reinforce the interpretation that the magmas responsible for these younger granitoids were also sourced from reworking of ancient crustal material.

S-type magmas are generally produced by the partial melting of metasedimentary rocks, particularly metapelites and metagraywackes, under water-deficient (water-undersaturated) conditions (e.g., Vielzeuf and Holloway, 1988; Pati˜no Douce and

476 Harris, 1998). The granitoids within the Jining and Helanshan complexes exhibit strong
477 peraluminosity, as indicated by A/CNK ratios greater than 1.1, and display elevated
478 zircon $\delta^{18}O$ values ranging from 7.3‰ to 11.6‰ (Dan et al., 2014; Wang et al., 2018).
479 These geochemical and isotopic characteristics are consistent with those of typical S-
480 type granites.

481 High $\varepsilon_{Hf}(t)$ values in zircon grains are widely interpreted as indicative of juvenile
482 continental sources (Jahn et al., 2000; Kemp et al., 2007; Kemp et al., 2005). The $\varepsilon_{Hf}(t)$
483 values data in the northern margin of Ordos Block (Fig. 14a) shows that 2.60–2.45 Ga
484 granitoids exhibit high $\varepsilon_{Hf}(t)$ values, while 2.40–2.10 Ga and 2.00–1.80 Ga granitoids
485 exhibit low $\varepsilon_{Hf}(t)$ values (Fig. 14a). Thus, 2.60–2.45 Ga I-type granitoids may represent
486 juvenile continental growth, while 2.45–2.30 Ga A-type granitoids and 1.88–1.80 Ga
487 A-type granitoids and S-type granitoids may represent the recycling of older crust.

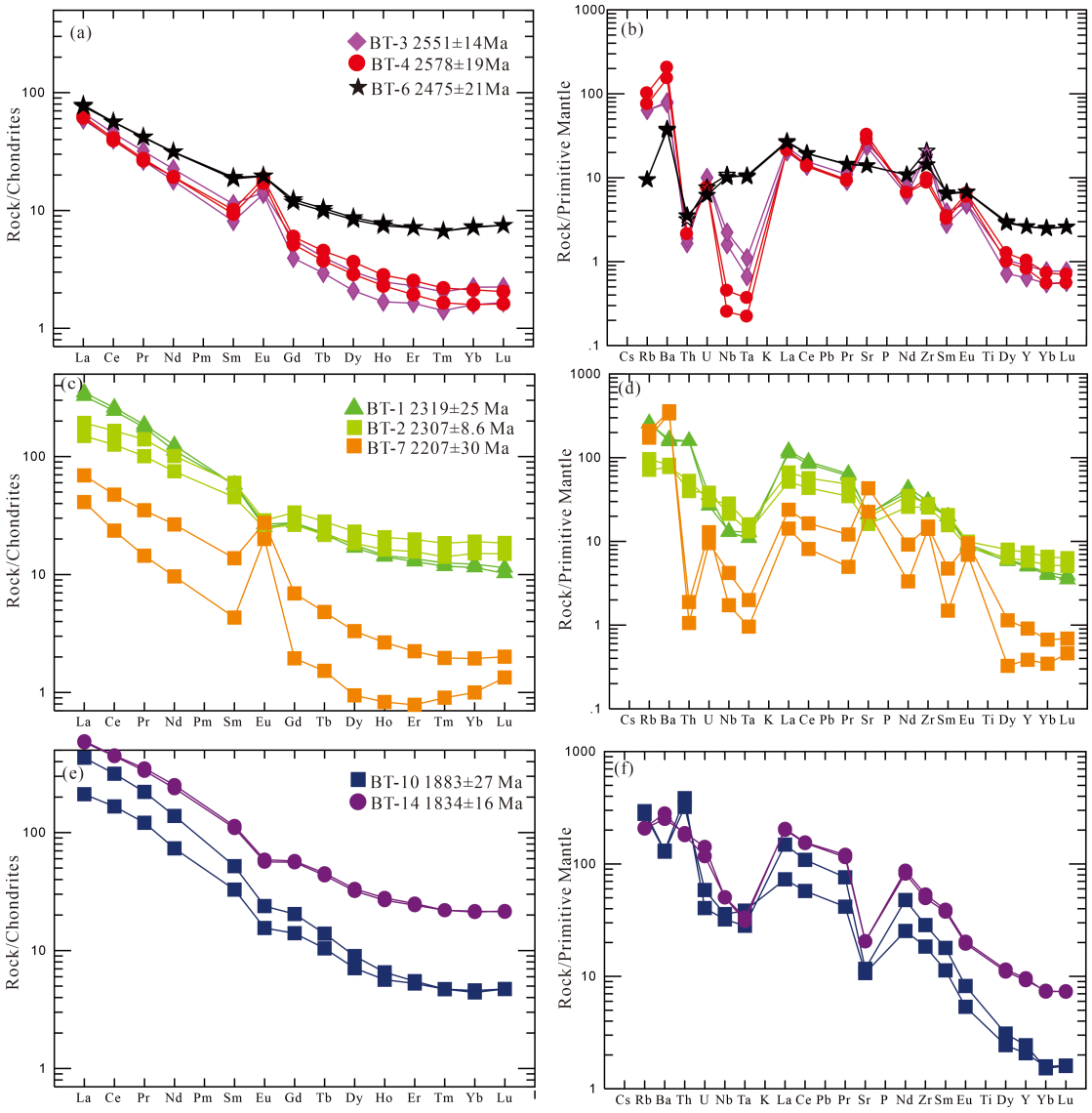

Fig. 12. Chondrite-normalized REE pattern (a) and primitive mantle-normalized trace elements spider diagram (b) for the whole-rock compositions of granitoids samples from the Daqingshan Complex (normalization values are from McDonough and Sun, 1995). Data sources are the same as in Fig. 11.

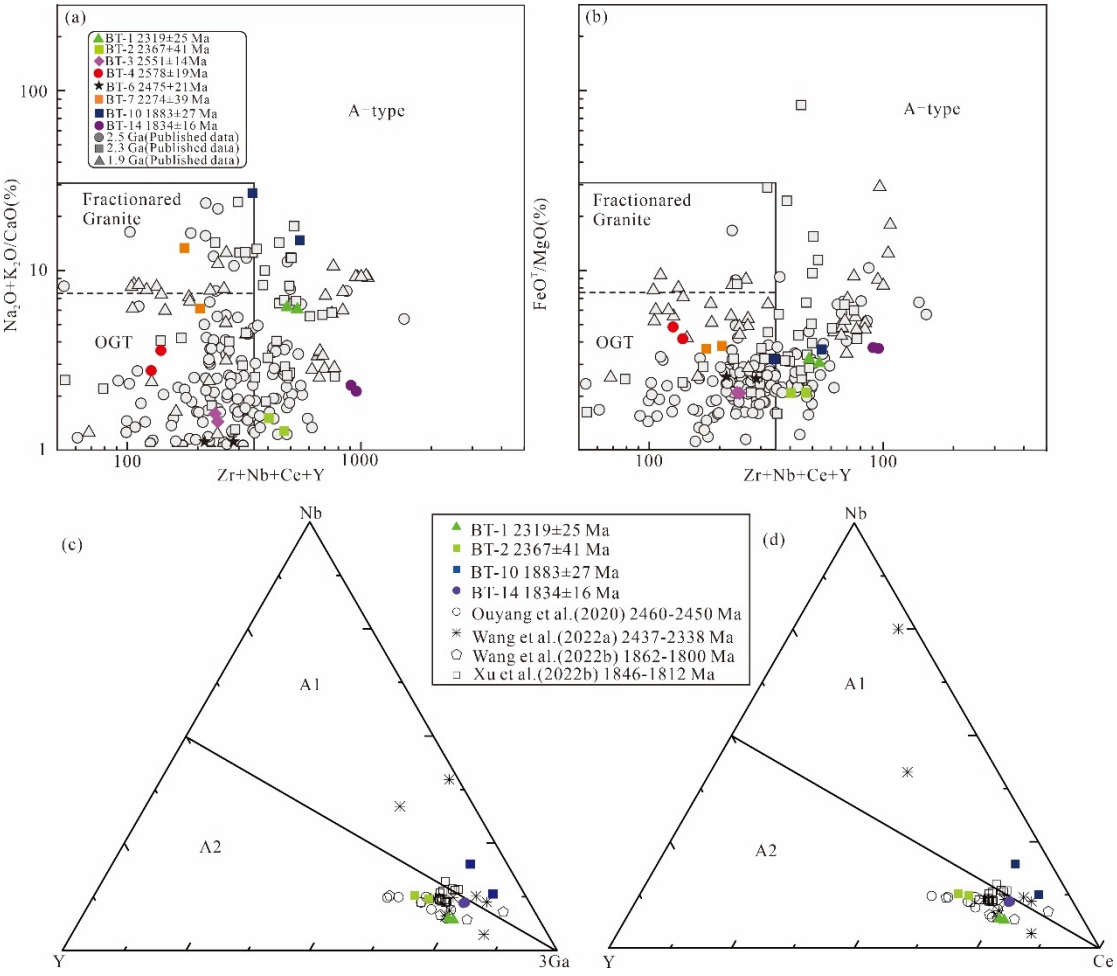

493

494 Fig. 13. (a) plots of (K_2O + Na_2O)/CaO vs Zr + Nb + Ce + Y (after Kamaunji et al., 2020); (b) plots

495 of (FeO^T/MgO)/CaO vs Zr + Nb + Ce + Y for the granitoids samples from the Daqingshan Complex;

496 (c) Plots of Y-Nb-3Ga Y-Nb-Ce and (d) Yb/Ta vs Y/Nb discrimination diagrams of the A1 and A2

497 subgroups (after Eby, 1992). Data sources are the same as in Fig. 11.

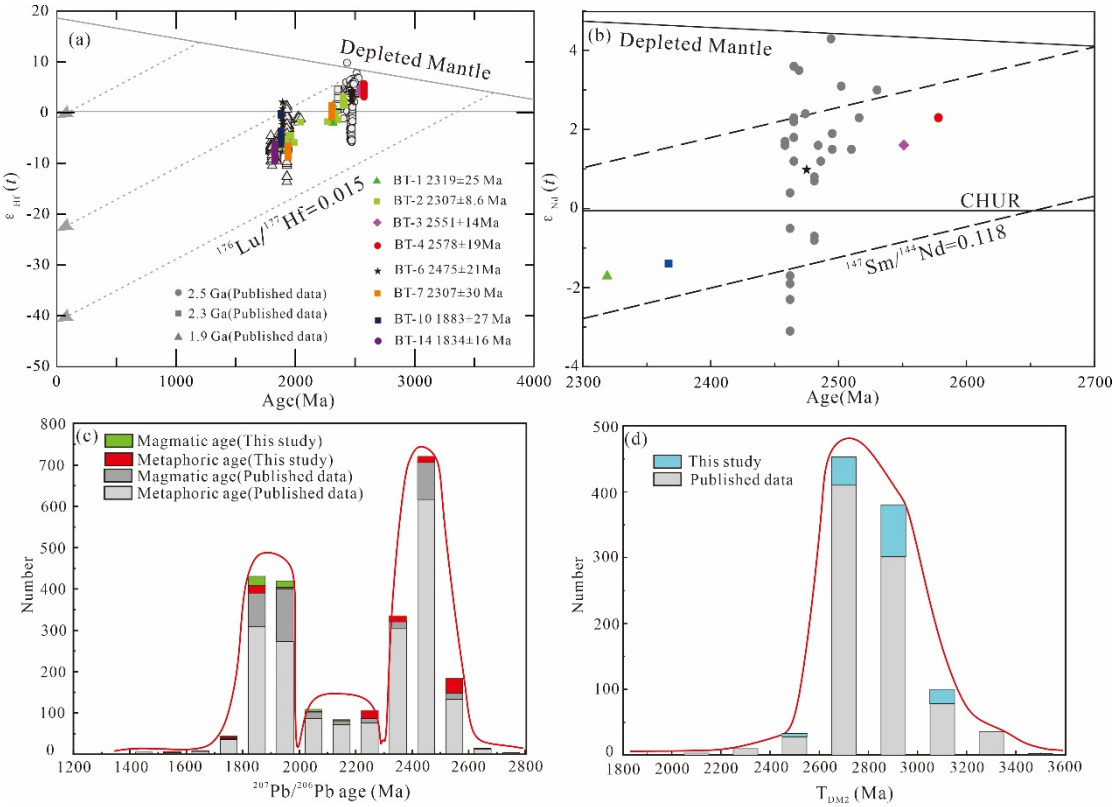

Fig. 14. (a) t-ε_{Hf}(t) diagram for zircon and (b) t-ε_{Nd}(t) for whole rock of the granitoids samples from the Daqingshan Complex. (c)$^{207}Pb/^{206}Pb$ ages diagrams and (d) Hf model ages (T_{DM2}) spectrums of zircons for granitoids in the KB and surrounding areas. Data sources from this study and ca. 2.60–2.45 Ga (Chen et al., 2017; Gao et al., 2021; Lian et al., 2023; Liu et al., 2017; Ma et al., 2013a; Ma et al., 2013b; Ma and Zhong, 2018; Ouyang and Guo, 2020; Ouyang et al., 2020; Zhang et al., 2011; Zhang et al., 2012; Zhang et al., 2023; Zhang et al., 2014); ca. 2.45–2.10 Ga (Dan et al., 2012; Wang et al., 2020; Wang et al., 2022a), ca. 2.0–1.80 Ga (Wang et al., 2018; Wang et al., 2022c; Xu et al., 2020)

4.3. Late Neoarchean-Proterozoic tectonic environment of the helium source rock

Previous studies have documented that the late Neoarchean granitoid gneisses from the northern margin of Ordos Block exhibit geochemical and geochronological characteristics consistent with Cordilleran I-type granitoids. These granitoids are interpreted to have formed through the partial melting of 2.7–3.0 Ga juvenile crust

(Dong et al., 2023; Liu et al., 2017; Wang et al., 2021). The geochemical characteristics and $\varepsilon_{Hf}(t)$ values of granitoid samples BT-3 and BT-4 are consistent with the features of calc-alkaline Cordilleran I-type granitoids. These data indicate that the granitoids were generated through the partial melting of juvenile basaltic crust, suggesting their formation within a tectonic environment characteristic of subduction-related juvenile magmatic arc systems (Murphy and Nance, 1991; Sengor et al., 1993). In this study, a Neoarchean crystallization age of 2578 ± 19 Ma was determined for the TTG granitoids in the Daqingshan area. This represents the earliest recorded arc-related magmatic event within the Khondalite Belt (KB), predating previously reported ages by Liu et al. (2017), Wang et al. (2021), and Dong et al. (2023). The findings indicate that initial subduction activity between the Yinshan and Ordos blocks began around 2.57 Ga. Furthermore, they indicate that plate tectonics governed the tectonic processes in this region during the Neoarchean.

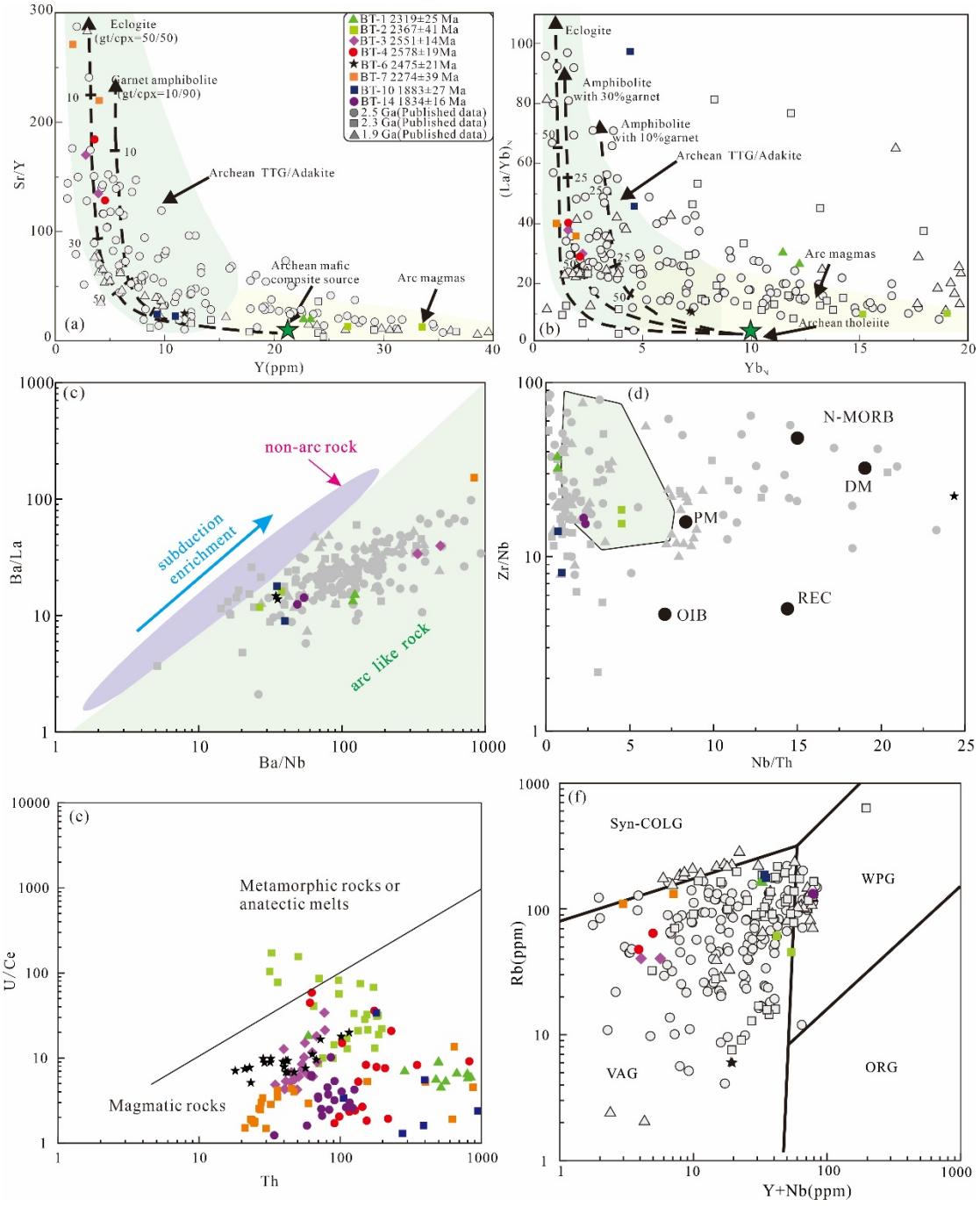

Fig. 15. (a) Sr/Y vs Y diagram (after Defant and Drummond, 1990); (b) $(La/Yb)_N$ vs Yb_N diagram (after Martin, 1986) (c) Ba/La vs. Ba/Nb (after Jenner et al., 2009); (d) Plots of Zr/Nb vs Nb/Th, deep depleted component (DEP), enriched component (EN), recycled component (REC), depleted component (DM) (after Condie, 2005); (e) Diagram of U/Ce ratio vs. Th concentration of zircons, separating magmatic from metamorphic zircons (after Wang et al., 2020) and (f) Y + Nb vs. Rb (after Pearce et al., 1984) for the granitoids samples from the Daqingshan Complex. Data sources are the same as in Fig. 11.

Ouyang and Guo (2020) documented the 2.48–2.46 Ga plutonic suite in the Daqingshan-Wulashan area. The dioritic-granitic rock associations from this period suggest nearly simultaneous melting of both mantle and crustal sources at varying depths, indicative of post-tectonic extension (Ouyang and Guo, 2020). The 2.46–2.45 Ga Jinpen gneissic granitoids from the Daqingshan area exhibit geochemical features typical of A2-type granites. These granitoids are interpreted to have formed through partial melting of pre-existing crustal rocks under high-temperature, low-pressure conditions, reflecting a tectonic regime shift from compression to extension and representing a critical phase in the initial cratonization of the North China Craton before approximately 2.45 Ga (Ouyang et al., 2020). The 2.42–2.35 Ga monzogranites in the Daqingshan area show the characteristics of Cordilleran I-type granitoids, suggesting their formation in a continental magmatic arc environment (Wang et al., 2022b). Coexisting 2.43-2.33 Ga A-type granitoids showing the coexistence of A1- and A2-type granitoids, indicative of continental arc magmatism within a rifting regime (Wang et al., 2022a). Combined samples BT-1, BT-2 with samples BT-7 showing the occurrence of A-type granite and I-type granite characteristics, indicating multiple magmatic arc events during 2.45–2.30 Ga. Our result is consistent with Wang et al. (2020, 2022a).

The 1.95–1.93 Ga granitoids display geochemical characteristics consistent with adakitic affinity and are interpreted to have formed through partial melting of a thickened ancient lower crust. These features reflect a significant tectonic transition in the Khondalite Belt during the late Paleoproterozoic, marking a shift from syn-collisional to post-collisional tectonic settings within the 1.95–1.93 Ga interval (Wang et al., 2022c). The geochemical signatures of the 1.86–1.80 Ga quartz monzonites from the Daqingshan area indicate that they were likely generated through the partial melting of Neoarchean-aged crustal material, particularly Neoarchean TTG rocks. This melting process was driven by elevated thermal input associated with the upwelling of mantle-derived magmas within a post-collisional extensional tectonic regime (Wang et al., 2022b). Overall, there are multiple magmatic events during 1.95-1.80 Ga, including

1.95-1.93 Ga adakitic granites and S-type granites (Dan et al., 2014; Wang et al., 2018; Wang et al., 2022c; Xu et al., 2020), 1.86-1.80 Ga A-type granites (Wang et al., 2022b; Xu et al., 2020), and ~1.87 Ga S-type granites (Yin et al., 2011; Yin et al., 2009). Our data, including samples BT-10, BT-14, further supports the above process, indicating the tectonic transition from continent-continent collisional setting to a post-collision extensional setting in the late Proterozoic.

Our new findings, integrated with previous studies, demonstrate that the Khondalite Belt (KB) comprises multiple magmatic arcs and experienced prolonged deposition and multi-phase metamorphism, resembling Phanerozoic subduction–accretionary orogens such as the Cordilleran accretionary orogen (Cawood et al., 2009; Liu et al., 2017; Wang et al., 2022a; Wang et al., 2021).

4.4 Overview of helium source rock of the Khondalite Belt in the NCC and worldwide

Khondalite Belts exhibits favorable areas for predicting the distribution of helium source rocks, as the Khondalites are high grade metapelitic rocks usually containing minerals with high U and Th content, accompanied by A-type granitoids and S-type granitoids.

Global khondalite belts (including khondalite rocks) are conspicuous around the world, such as Kerala Khondalite belt of southern India (Morimoto et al., 2004), Highland Complex of Sri Lanka (Sajeev and Osanai, 2004), Jequie Block, Bahia in Brazil (Barbosa et al., 2006), Claudio Shear Zone in southern Sao Francisco craton(Brazil) (Coelho et al., 2019), Skallevikshalsen, Lutzo-Holm Complex (Kawakami and Motoyoshi, 2004) and Rundvagshetta, Lutzow-Holm Complex in East Antarctica and Khondalite belts in North China Craton (Kou et al., 2017; Li et al., 2014; Qiu et al., 2017; Santosh et al., 2006b; Wang et al., 2018, Xu et al, 0214).

Santosh et al. (2006a) summarized the geochronology of the khondalite belt of Trivandrum Block, Southern India and the Electron probe ages indicate that the metasediments were derived from Archean to Paleo-Mesoproterozoic crustal components, which likely accreted during the assembly of ancient supercontinents such as Ur and Columbia. Liu et al. (2016) pointed out that the khondalite precursor sediments of Trivandrum Block were deposited more than 2.1 Ga ago. The southern Indian khondalites represent a segment of an extensive Palaeoproterozoic metasedimentary belt that potentially formed a continuous depositional system extending from southern Madagascar through the Trivandrum Block to Sri Lanka's Highland Complex. This metasedimentary package exhibits characteristics typical of a passive continental margin sequence, likely developed along the southern periphery of the Archaean to early Palaeoproterozoic Dharwar craton (Dharmapriya et al., 2014; Liu et al, 2016).

The Khondalite in Brazil is in the dextral Claudio shear zone (CSZ) in southern Sao Francisco craton (SFC). The metamorphic setting of the CSZ khondalitic paragneisses is characterized by a metamorphic peak of 900–950 °C and 10–11 kbar and monazite U-Th-Pb geochronology constrains two distinct metamorphic events: (1) peak metamorphism at 2011 ± 20 Ma, and (2) post-peak retrograde stage at 1910 ± 20 Ma, delineating a ~100 Myr tectonothermal evolution (Coelho et al., 2019). The Khondalite in CSV exhibit similar P and T evolution to the Wulashan Complex from North China Craton (NCC). The khondalitic rocks of both CSZ and Wulashan Complex were subjected to a clockwise P-T-t path granulite facies metamorphism accompanied by partial melting events when SFC and NCC were probably connected during Paleoproterozoic. (Cai et al., 2016; Coelho et al., 2019). The evidences indicate that global khondalite belts formed synchronously under similar tectonic settings.

By comparison of U and Th content in Khondalite Belt (NCC) with global Khondalite Belts, we found that global Khondalite belts, containing Khondalit

e Belt (NCC), Khondalite belts in Southern India and Khondalite belts in Sout hern Sao Francisco craton (Brazil) exhibit high U and Th contents, which are comparable to the three types granitoids of helium source rock in this study(Fi g. 16). Thus, we propose that global Khondalite belts holds significant scientifi c value for predicting the worldwide distribution of helium source rocks.

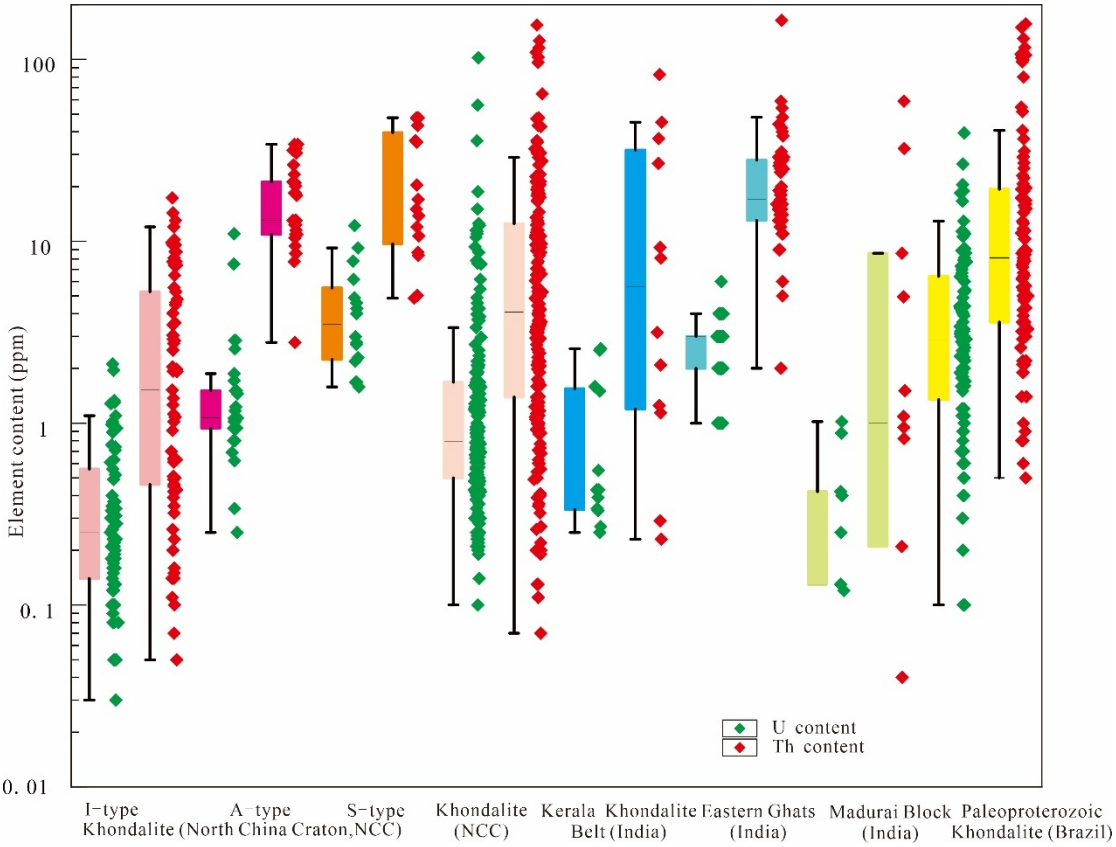

Fig. 16. Comparison of U and Th content in Khondalite Belt (NCC) with global Khondali te Belts. Data sources: Khondalite (NCC) (Kou et al., 2017; Li et al., 2014; Qiu et al., 2 017; Wang et al., 2018, Xu et al, 0214);Kerala Khondalite (India) (Kroner et al., 2015); E astern Ghats (India) (Dash et al., 1987); Madurai Block (Plavsa et al.,2012); Paleoproteroz oic Khondalite (Brazil) (Cuadros et al.,2017)

4.5 The accumulation mechanism of U and Th in the Northern Ordos Block

Uranium (U) and thorium (Th), being strongly incompatible elements, exhibit low partition coefficients and preferentially partition into the melt phase during partial melting. Consequently, these elements become enriched in the upper crust through melt

632 migration processes. Large tracts of strongly differentiated crust formed at ca 3.0–2.5
633 Ga, which contains abundant granitoid rocks with elevated concentrations of U, Th and
634 K (Laurent et al., 2014; Schoene et al., 2008). The 2.60–2.45 Ga I-type granitoids were
635 derived from a juvenile crustal source and consequently exhibit elevated concentrations
636 of uranium (U) and thorium (Th). In contrast, the S-type granitoids originated from the
637 partial melting of ancient metasedimentary rocks. Early subaerial weathering led to the
638 concentration of uranium (U) and thorium (Th) in terrigenous sediments, which
639 subsequently lithified into metasedimentary rocks. Through ancient crustal recycling
640 processes, U and Th ultimately became enriched in the S-type granitoids. In addition,
641 the 2.0–1.9 Ga paragneiss in the northern Ordos also exhibits elevated uranium (U) and
642 thorium (Th) concentrations (Tian et al., 2025), consistent with the enrichment
643 mechanism proposed for the S-type granitoids. Clay minerals, such as montmorillonite,
644 kaolinite, and illite, within terrigenous sediments exhibit strong adsorption capabilities
645 for uranium (U) and thorium (Th) due to their unique layered structures and surface
646 properties. In this context, U and Th, along with potassium (K), were incorporated into
647 the deep crust through subduction, leading to the formation of high-potassium magmas
648 in the upper crust. Through ancient crustal recycling processes, U, Th, and K were
649 ultimately enriched in A-type granitoids. We propose that multiple cycles of ancient
650 crustal recycling serve as the primary mechanism for the enrichment of uranium (U)
651 and thorium (Th) in basement rocks (Fig. 17). The differentiation of the ancient crust
652 led to the formation of A-type and S-type granitic gneiss, suggesting that peraluminous
653 and high-potassium magmas in the upper crust are the initial contributors to U and Th
654 enrichment (Fig. 17).

655 The enrichment patterns of uranium (U) and thorium (Th) in northern Ordos Block
656 could be concluded as following process. Subaerial weathering concentrated U and Th
657 into terrigenous sediments within metasedimentary rocks before 2.52 Ga (Wang and
658 Guo, 2017). These terrigenous sediments with high U and Th content were incorporated
659 into the deep crust through subduction, where they experienced crustal melting.

Subsequent melt-migration redistributed the U and Th from the lower to the upper crust, forming potassic and peraluminous magmas. Therefore, the S-type granitoids and A-type granitoids originated from potassic and peraluminous magmas through ancient crustal recycling. Reimink and Smye (2024) propose a thermodynamic model for stabilization of continents and their conclusions from the perspective of radiogenic heat production reach an agreement with this study. It is the long-term arc-continent accretion, containing terrigenous sediments with high U and Th content experiencing multistage crustal recycling, that explains why U and Th are enriched in the helium source rocks, which widely distributed in the Northern Ordos Block.

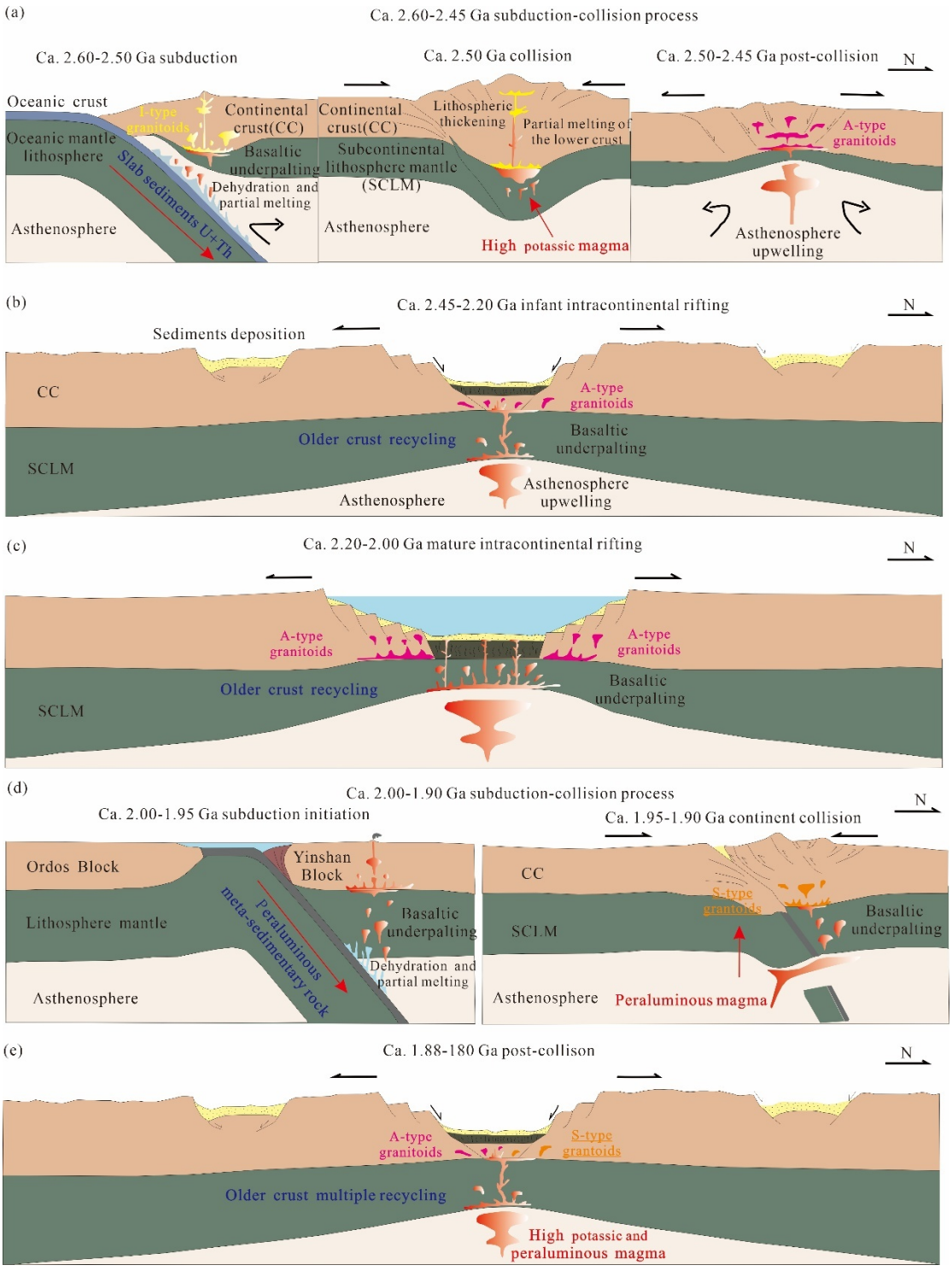

Fig. 17. The accumulation mechanism of U and Th in the Northern Ordos Block (Modified after Ouyang and Guo, 2020; Lian et al., 2023)

5. Conclusions

(1) Late Neoarchean–Paleoproterozoic granitoids, consisting of 2.60–2.45 Ga I-

type granitoids, 2.45–2.30 Ga A-type granitoids and I-type granitoids and 1.95–1.80 Ga S-type granitoids and A-type granitoids, are believed to be effective helium source rock type in the north Ordos Block. Based on the EPMA, monazite is considered to be the dominate associated mineral from the effective helium source rock type.

(2) The northern Ordos Block experienced 2.60–2.45 Ga late Archean subduction-accretion and arc magmatism, 2.45–2.30 Ga arc-continental accretion process with multiple continental arc magmatism and 1.95–1.80 Ga tectonic transition from continent-continent collision setting to post-collisional extension setting. By comparison of Khondalite Belt (NCC) with global Khondalite Belts, global Khondalite belts could be favorable areas for predicting the worldwide distribution of helium source rocks.

(3) It is the long-term arc-continent accretion, containing terrigenous sediments with high U and Th content experiencing multistage crustal recycling, analogous to Phanerozoic subduction–accretionary orogens such as the Cordilleran accretionary orogen, that explains why effective helium source rocks are widely distributed in the Northern Ordos Block.

690 References

691 Akhtar, S., Yang, X., Pirajno, F., 2017. Sandstone type uranium deposits in the Ordos Block, Northwest
692 China: A case study and an overview. Journal of Asian Earth Sciences 146, 367-382.
693 Altherr, R., Holl, A., Hegner, E., Langer, C., Kreuzer, H., 2000. High-potassium, calc-alkaline I-type
694 plutonism in the European Variscides: northern Vosges (France) and northern Schwarzwald
695 (Germany). Lithos 50, 51-73.
696 Anderson, J.L., 1983. Proterozoic anorogenic granite plutonism of North America. Geological Society
697 of America 34, 134-154.
698 Ballentine, C.J., Burnard, P.G., 2002. Production, Release and Transport of Noble Gases in the
699 Continental Crust. Reviews in Mineralogy & Geochemistry 47, 481-538.
700 Ballentine, C.J., Sherwood Lollar, B., 2002. Regional groundwater focusing of nitrogen and noble gases
701 into the Hugoton-Panhandle giant gas field, USA. Geochimica et Cosmochimica Acta 66, 2483-
702 2497.
703 Barbosa, J., Nicollet, C., Leite, C., Kienast, J.R., Fuck, R.A., Macedo, E.P., 2006. Hercynite-qu
704 artz-bearing granulites from Brejoes Dome area, Jequie Block,Bahia, Brazil: influence of c
705 harnockite intrusion on granulite facies metamorphism. Lithos 92, 537–556.
706 Bogaerts, M., Scaillet, B., Auwera, J.V., 2006. Phase equilibria of the Lyngdal granodiorite (Norway):
707 implications for the origin of metaluminous ferroan granitoids. Journal of Petrology 47, 2405-2431.
708 Bonin, B., 2007. A-type granites and related rocks: evolution of a concept, problems and prospects.
709 Lithos 97, 1-29.
710 Broadhead, R.F., 2005. Helium in New Mexico-geologic distribution, resource demand, and exploration
711 possibilities. New Mexico Geology 27, 93-101.
712 Brown, A., 2010. Formation of High Helium Gases: A Guidefor Explorationists. AAPGConvention,
713 Louisianal, New OrleG ans, USA.
714 Cawood, P.A., Kröner, A., Collins, W.J., Kusky, T.M., Mooney, W.D., Windley, B.F., 2009. Accretionary
715 orogens through Earth history. Geological Society, London, Special Publications 318, 1-36.
716 Chen, N.H.-C., Zhao, G., Sun, M., Zhou, H., 2017. Geochemistry of ~2.5Ga granitoids at the northern
717 margin of the Yinshan Block: Implications for the crustal evolution of the North China Craton.
718 Precambrian Research 303, 673-686.
719 Chen, Y., Jin, R., Miao, P., Li, J., Guo, H., Chen, L., 2019. Occurrence of pyrites in sandstone-type
720 uranium deposits: Relationships with uranium mineralization in the North Ordos Block, China. Ore
721 Geology Reviews 109, 426-447.
722 Coelho, R.M., Chaves, A.d.O., 2019. Pressure-temperature-time path of Paleoproterozoic khondal
723 ites from Claudio shear zone (southern São Francisco craton, Brazil): Links with khondalit
724 e belt of the North China craton. Journal of South American Earth Sciences 94, 102250.
725 Collins, W.J., Beams, S.D., White, A., Chappell, B., 1982. Nature and origin of A-type granites with
726 particular reference to southeastern Australia. Contributions to mineralogy and petrology 80, 189-
727 200.
728 Creaser, R.A., Price, R.C., Wormald, R.J., 1991. A-type granites revisited: assessment of a residual-

source model. Geology 19, 163-166.
Cuadros, F.A., Botelho, N.F., Fuck, R.A., Dantas, E.L., 2017. The peraluminous Aurumina Granite Suite in central Brazil: An example of mantle-continental crust interaction in a Paleoproterozoic cordilleran hinterland setting? Precambrian Research 299, 75-100.
Dai, J., Ni, Y., Qin, S., Huang, S., Gong, D., Liu, D., Feng, Z., Peng, W., Han, W., Fang, C., 2017. Geochemical characteristics of He and CO2 from the Ordos (cratonic) and Bohaibay (rift) basins in China. Chemical Geology 469, 192-213.
Dai, S., Jiang, Y., Ward, C.R., Gu, L., Seredin, V.V., Liu, H., Zhou, D., Wang, X., Sun, Y., Zou, J., 2012. Mineralogical and geochemical compositions of the coal in the Guanbanwusu Mine, Inner Mongolia, China: Further evidence for the existence of an Al (Ga and REE) ore deposit in the Jungar Coalfield. International Journal of Coal Geology 98, 10-40.
Dan, W., Li, X.-H., Guo, J., Liu, Y., Wang, X.-C., 2012. Paleoproterozoic evolution of the eastern Alxa Block, westernmost North China: Evidence from in situ zircon U–Pb dating and Hf–O isotopes. Gondwana Research 21, 838-864.
Dan, W., Li, X.-H., Wang, Q., Wang, X.-C., Liu, Y., Wyman, D.A., 2014. Paleoproterozoic S-type granites in the Helanshan Complex, Khondalite Belt, North China Craton: Implications for rapid sediment recycling during slab break-off. Precambrian Research 254, 59-72.
Dan, W., Li, X.-H., Wang, Q., Wang, X.-C., Liu, Y., Wyman, D.A., 2014. Paleoproterozoic S-type granites in the Helanshan Complex, Khondalite Belt, North China Craton: Implications for rapid sediment recycling during slab break-off. Precambrian Research 254, 59-72.
Dharmapriya, P.L., Malaviarachchi, S.P.K., Galli, A., Su, B.-X., Subasinghe, N.D., Dissanayake, C.B., Nimalsiri, T.B., Zhu, B., 2014. P–T evolution of a spinel+quartz bearing khondalite from the Highland Complex, Sri Lanka: Implications for non-UHT metamorphism. Journal of Asian Earth Sciences 95, 99-113.
Dong, C., Li, P., Liu, S., Ma, M., Wan, Y., Wilde, S.A., Xie, S., Xu, Z., 2023. Establishing the occurrence of late Neoarchaean – earliest Palaeoproterozoic magmatism in the Daqingshan area, northwestern North China Craton: SIMS U–Pb zircon dating, Lu–Hf and Sm–Nd isotopes and whole-rock geochemistry. Geological Magazine 160, 732-754.
Eby, G.N., 1992. Chemical subdivision of the A-type granitoids: petrogenetic and tectonic implications. Geology 20, 641-644.
Frost, B.R., Barnes, C.G., Collins, W.J., Arculus, R.J., ELLIS, D.J., Frost, C.D., 2001. A Geochemical Classification for Granitic Rocks. Journal of Petrology 42, 2033-2048.
Frost, C., Frost, B., Chamberlain, K., Edwards, B., 1999. Petrogenesis of the 1.43 Ga Sherman batholith, SE Wyoming, USA: a reduced, rapakivi-type anorogenic granite. Journal of petrology 40, 1771-1802.
Frost, C.D., Frost, B.R., 2011. On ferroan (A-type) granitoids: their compositional variability and modes of origin. Journal of petrology 52, 39-53.
Frost, C.D., Ronald Frost, B., 1997. Reduced rapakivi-type granites: the tholeiite connection. Geology 25, 647-650.
Gao, M., Zhang, Z.-J., Cheng, Q.-M., Grujic, D., 2021. Zircon U-Pb and Lu-Hf isotopes of Huai'an complex granites, North China Craton: Implications for crustal growth, reworking and tectonic evolution. Gondwana Research 90, 118-134.

Gao, Y., Liu, Q., Wu, X., Zhu, D., Li, P., 2023. Research on the difference of crustal helium accumulation in Dongsheng and Daniudi gas fields, Ordos Block. Natural Gas Geoscience 34, 1790-1800.

Gold, T., Held, M., 1987. Helium-nitrogen-methane systematics in natural gases of Texas and Kansas. Journal of Petroleum Geology 10, 415-424.

Guo, J., Peng, P., Chen, Y., Jiao, S., Windley, B.F., 2012. UHT sapphirine granulite metamorphism at 1.93–1.92 Ga caused by gabbronorite intrusions: implications for tectonic evolution of the northern margin of the North China Craton. Precambrian Research 222, 124-142.

He, F., Wang, J., Zhao, Y., An, C., Wang, F., Tao, C., Ni, C., Jia, H., 2022. Accumulation characteristics of Dongsheng helium-rich gas field in Ordos Block and its tectonic background. Journal of Palaeogeography 24, 937-950.

Hui, J., Kang, R., Zhao, W., Fan, L., Jia, L., Ji, H., Wang, Y., 2024. Helium characteristics and potential in the Ordos Block. Natural Gas Geoscience 35, 1688-1698.

Jahn, B.M., Wu, F., Chen, B., 2000. Granitoids of the Central Asian Orogenic Belt and continental growth in the Phanerozoic. Earth and Environmental Science Transactions of the Royal Society of Edinburgh 91, 181-193.

Ji, W., Li, W., Liu, Z., Lei, T., 2013. Research on the Upper Paleozoic Gas Source of the Hangjinqi Block in the Northern Ordos Block. Natural Gas Geoscience 24, 905-914.

Jiao, S., Guo, J., Harley, S.L., Peng, P., 2013. Geochronology and trace element geochemistry of zircon, monazite and garnet from the garnetite and/or associated other high-grade rocks: Implications for Palaeoproterozoic tectonothermal evolution of the Khondalite Belt, North China Craton. Precambrian Research 237, 78-100.

Jiao, S.J., Guo, J.H., Wang, L.J., Peng, P., 2015. Short-lived high-temperature prograde and retrograde metamorphism in Shaerqin sapphirine-bearing metapelites from the Daqingshan terrane, North China Craton. Precambrian Research 269, 31-57.

Johnson, E.G., 2012. Helium in Northeastern British Columbia. Geoscience Reports 2013, British Columbia Ministry of Natural Gas Development, 5, 45–52

Kärenlampi, K., Heinonen, J.S., Kontinen, A., Hanski, E., Huhma, H., 2021. Geochemical and thermodynamic modeling of the petrogenesis of A1-type granites and associated intermediate rocks: A case study from the central Fennoscandian Shield. Geochemistry 81, 125734.

Kawakami, T., Motoyoshi, Y., 2004. Timing of attainment of the spinel + quartz,coexistence in garnet–sillimanite leucogneiss fromSkallevikshalsen, Lutzow-Holm complex, East Antarctic a. Journal of Mineralogical and Petrological Sciences 99, 311-319.

Kelley, D.S., Karson, J.A., Früh-Green, G.L., Yoerger, D.R., Shank, T.M., Butterfield, D.A., Hayes, J.M., Schrenk, M.O., Olson, E.J., Proskurowski, G., Jakuba, M., Bradley, A., Larson, B., Ludwig, K., Glickson, D., Buckman, K., Bradley, A.S., Brazelton, W.J., Roe, K., Elend, M.J., Delacour, A., Bernasconi, S.M., Lilley, M.D., Baross, J.A., Summons, R.E., Sylva, S.P., 2005. A Serpentinite-Hosted Ecosystem: The Lost City Hydrothermal Field. Science 307, 1428-1434.

Kemp, A., Hawkesworth, C.J., Foster, G., Paterson, B., Woodhead, J., Hergt, J., Gray, C., Whitehouse, M., 2007. Magmatic and crustal differentiation history of granitic rocks from Hf-O isotopes in zircon. Science 315, 980-983.

Kemp, A., Wormald, R., Whitehouse, M., Price, R., 2005. Hf isotopes in zircon reveal contrasting sources and crystallization histories for alkaline to peralkaline granites of Temora, southeastern Australia.

Geology 33, 797-800.
Kusky, T., Mooney, W., 2015. Is the Ordos Block floored by a trapped oceanic plateau? Earth and Planetary Science Letters 429, 197-204.
Laurent, O., Martin, H., Moyen, J.-F., Doucelance, R., 2014. The diversity and evolution of late-Archean granitoids: Evidence for the onset of "modern-style" plate tectonics between 3.0 and 2.5 Ga. Lithos 205, 208-235.
Li, J., Li, Y., Hu, S., Zhou, J., Chen, G., Zhang, S., 2022. "Shanxi-type" helium accumulation model and its essentiality. Journal of Xi'an University of Science and Technology 42, 529-536.
Li, W., Dong, Y., Liu, X., 2018. Geochronology, geochemistry and Nd–Hf isotopes of the Xiao kouzi granite from the Helanshan complex: constraints on the Paleoproterozoic evolution o f the Khondalite Belt, North China Craton. Precambrian Research 317, 57-76.
Li, W., Yin, C., Lin, S., Li, W., Gao, P., Zhang, J., Qian, J., Qiao, H., 2022. Paleoproterozoic tectonic evolution from subduction to collision of the Khondalite Belt in North China: Evi dence from multiple magmatism in the Qianlishan Complex. Precambrian Research 368, 10 6471.
Li, W.Q., Liu, H.C., Holland, G., Zhou, Z., Chen, J.F., Li, J., Wang, X.B., 2024. Accumulation mechanism of crust–mantle mixing helium-rich reservoir: a case study of the Subei basin (Eastern China). International Geology Review, online.
Li, X.P., Yang, Z., Zhao, G., Grapes, R., Guo, J., 2011. Geochronology of khondalite-series rocks of the Jining Complex: confirmation of depositional age and tectonometamorphic evolution of the North China craton. International Geology Review 53, 1194-1211.
Lian, G., Xu, Z., Liu, Z., Liu, J., Li, P., Gong, Y., Li, S., 2023. Neoarchean to Paleoproterozoic tectonic evolution of the Khondalite Belt in the North China Craton: Constraints from ca. 2.5 Ga and ca. 2.1 Ga charnockites in Zhuozi. Precambrian Research 396, 107167.
Liu, H., Li, X.P., Kong, F.M., Santosh, M., Wang, H., 2019. Ultra-high temperature overprinting of high pressure pelitic granulites in the Huai'an complex, North China Craton: Evidence from thermodynamic modeling and isotope geochronology. Gondwana Research 72, 15-33.
Liu, H., Li, X.P., Kong, F.M., Schertl, H.P., Ma, S.T., Wang, X.M., 2021. An early high-pressure history preceeded pelitic ultrahigh-temperature granulite formation in the Tuguiwula area, Khondalite Belt, North China Craton. Precambrian Research 357, 106123.
Liu, J., Liu, F., Ding, Z., Liu, P., Chen, J., Liu, C., Wang, F., Yang, H., Cai, J., Shi, J., 2017. Late Neoarchean–Paleoproterozoic arc-continent accretion along the Khondalite Belt, Western Block, North China Craton: Insights from granitoid rocks of the Daqingshan–Wulashan area. Precambrian Research 303, 494-519.
Liu, Q., Jin, Z., Wang, Y., Han, P., Tao, Y., Wang, Q., Ren, Z., Li, W., 2012. Gas filling pattern in Paleozoic marine carbonate reservoir of Ordos Block. Acta Petrologica Sinica 28, 847-858.
Liu, Q., Wu, X., Jia, H., Ni, C., Zhu, J., Miao, J., Zhu, D., Meng, Q., Peng, W., Xu, H., 2022. Geochemical characteristics of helium in natural gas from the Daniudi gas field, Ordos Block, central China. Frontiers in Earth Science 10, 823308.
Liu, S., Kröner, A., Wan, Y., Santosh, M., Shaji, E., Dhanil Dev, S.G., 2016. Late Palaeoproter ozoic depositional age for khondalite protoliths in southern India and tectonic implications. Precambrian Research 283, 50-67.

Liu, W., Pan, H., Li, J., Zhao, J., 2015. Well logging evaluation on bauxitic mudstone reservoirs in theDaniudi Gasfield, Ordos Block. Natural Gas Industry 35, 24-30.

Loiselle, M., 1979. Characteristics and origin of anorogenic granites. Geological Society of America 11, 468-495.

Ma, X., Fan, H.-R., Santosh, M., Guo, J., 2013a. Geochemistry and zircon U–Pb chronology of charnockites in the Yinshan Block, North China Craton: tectonic evolution involving Neoarchaean ridge subduction. International Geology Review 55, 1688-1704.

Ma, X., Guo, J., Liu, F., Qian, Q., Fan, H., 2013b. Zircon U–Pb ages, trace elements and Nd–Hf isotopic geochemistry of Guyang sanukitoids and related rocks: Implications for the Archean crustal evolution of the Yinshan Block, North China Craton. Precambrian Research 230, 61-78.

Ma, X., Zhong, Y., 2018. Geochemistry and chronology of a diorite pluton in the Yinshan Block, implications for crustal growth and evolution of North China Craton. Geological Journal 53, 2849-2862.

Middlemost, E.A.K., 1994. Naming materials in the magma/igneous rock system. Earth-Science Reviews 37, 215-224.

Mingram, B., Trumbull, R., Littman, S., Gerstenberger, H., 2000. A petrogenetic study of anorogenic felsic magmatism in the Cretaceous Paresis ring complex, Namibia: evidence for mixing of crust and mantle-derived components. Lithos 54, 1-22.

Morimoto, T., Santosh, M., Tsunogae, T., Yoshimura, Y., 2004. Spinel + quartzassociation from the Kerala khondalites, southern India: evidence for ultra high temperature metamorphism. Journal of Mineralogical and Petrological Sciences 99, 257-278.

Ni, Y., Dai, J., Tao, S., Wu, X., Liao, F., Wu, W., Zhang, D., 2014. Helium signatures of gases from the Sichuan Basin, China. Organic geochemistry 74, 33-43.

Nikonov, V., 1973. Formation of helium-bearing gases and trends in prospecting for them. International Geology Review 15, 534-541.

Ouyang, D., Guo, J., 2020. Modern-style tectonic cycle in earliest Proterozoic time: Petrogenesis of dioritic-granitic rocks from the Daqingshan–Wulashan Terrane, southern Yinshan Block, North China Craton. Lithos 352-353, 105322.

Ouyang, D., Guo, J., Liou, P., Huang, G., 2020. Petrogenesis and tectonic implications of 2.45 Ga potassic A-type granite in the Daqingshan area, Yinshan Block, North China Craton. Precambrian Research 336, 105435.

Patiño Douce, A.E., 1997. Generation of metaluminous A-type granites by low-pressure melting of calc-alkaline granitoids. Geology 25, 743-746.

Peng, P., Guo, J., Windley, B., Liu, F., Chu, Z., Zhai, M., 2012. Petrogenesis of Late Paleoproterozoic Liangcheng charnockites and S-type granites in the central-northern margin of the North China Craton: implications for ridge subduction. Precambrian Research 222, 107-123.

Peng, W., Quanyou, L., Ying, Z., Huichong, J., Dongya, Z., Qingqiang, M., Xiaoqi, W., Shang, D., Yongsheng, M., 2022. The first extra-large helium-rich gas field identified in a tight sandstone of the Dongsheng Gas Field, Ordos Block, China. Science China-Earth Sciences 65, 874–881.

Pierce, A., Gott, G., Mytton, J., 1964. Uranium and helium in the Panhandle gas field. Texas, and adjacent areas. US Geological Survey Professional Paper, 57, 484-512.

Plavsa, D., Collins, A.S., Foden, J.F., Kropinski, L., Santosh, M., Chetty, T.R.K., Clark, C., 20

12. Delineating crustal domains in Peninsular India: Age and chemistry of orthopyroxene-bearing felsic gneisses in the Madurai Block. Precambrian Research 198-199, 77-93.
Plavsa, D., Collins, A.S., Payne, J.L., Foden, J.D., Clark, C., Santosh, M., 2014. Detrital zircons in basement metasedimentary protoliths unveil the origins of southern India. GSA Bulletin 126, 791-811.
Reimink, J.R., Smye, A.J., 2024. Subaerial weathering drove stabilization of continents. Nature 629, 609-615.
Ruedemann, P., Oles, L., 1929. Helium--Its Probable Origin and Concentration in the Amarillo Fold, Texas. AAPG Bulletin 13, 799-810.
Sajeev, K., Osanai, Y., 2004. Osumilite and spinel + quartz from Sri Lanka: implications for UHT conditions and retrograde P–T path. Journal of Mineralogical and Petrological Sciences 99, 320-327.
Santosh, M., Morimoto, T., Tsutsumi, Y., 2006a. Geochronology of the khondalite belt of Trivandrum Block, Southern India: Electron probe ages and implications for Gondwana tectonics. Gondwana Research 9, 261-278.
Santosh, M., Sajeev, K., Li, J.H., 2006b. Extreme crustal metamorphism during Colombia supercontinent assembly: evidence from North China Craton. Gondwana Research. 10, 256-266.
Santosh, M., Wan, Y., Liu, D., Chunyan, D., Li, J., 2009. Anatomy of zircons from an ultrahot orogen: the amalgamation of the North China craton within the supercontinent Columbia. The Journal of Geology 117, 429-443.
Santosh, M., Wilde, S., Li, J., 2007. Timing of Paleoproterozoic ultrahigh-temperature metamorphism in the North China Craton: evidence from SHRIMP U–Pb zircon geochronology. Precambrian Research 159, 178-196.
Schoene, B., de Wit, M.J., Bowring, S.A., 2008. Mesoarchean assembly and stabilization of the eastern Kaapvaal craton: A structural-thermochronological perspective. Tectonics 27, 1-27.
Shi, Q., Shu, R.-X., Chen, X.-Z., Zhao, G.-C., Chen, Y.-S., Wang, Z.-S., Ma, L., Xu, Z.-Y., Liu, Z.-H., Chen, K.-Y., 2025. Paleoproterozoic granite in the Khondalite Belt, northern margin of the North China Craton: Response to the assembly of the Columbia supercontinent. Precambrian Research 417, 107640.
Skjerlie, K.P., Johnston, A.D., 1993. Fluid-absent melting behavior of an F-rich tonalitic gneiss at mid-crustal pressures: implications for the generation of anorogenic granites. Journal of Petrology 34, 785-815.
Tao, X., Li, J., Zhao, L., Li, L., Zhu, W., Xing, L., Su, F., Shan, X., Zheng, H., Zhang, L., 2019. Helium resources and discovery of first supergiant helium reserve in China: Hetianhe Gas Field. Journal of Earth Science 44, 1024-1041.
Taylor, S.R., McLennan, S.M., 1995. The geochemical evolution of the continental crust. Reviews of geophysics 33, 241-265.
Tian, G., Yang, M., Ma, L., Song, L., Wen, X., Xue, H., Jia, H., Pu, R., Chen, J., Chen, S., 2025. A Buried Columbia-Forming Orogen Front Located in the Northwestern North China Craton. Tectonics 44, 1-22.
Tian, G., Yang, M., Song, L., Jia, H., Liu, H., Zhang, S., Zhang, W., Xing, Z., Chen, J., Bai, D., Li, J., 2023. Late Neoarchean plate subduction in Western North China Craton: Evidence from ca. 2.51

939 Ga to 2.46 Ga basement rocks in Northern Ordos Block. Precambrian Research 387, 106979.
940 Turner, S.P., Foden, J.D., Morrison, R., 1992. Derivation of some A-type magmas by fractionation of
941 basaltic magma: an example from the Padthaway Ridge, South Australia. Lithos 28, 151-179.
942 Vander Auwera, J., Bogaerts, M., Liégeois, J.-P., Demaiffe, D., Wilmart, E., Bolle, O., Duchesne, J.C.,
943 2003. Derivation of the 1.0–0.9 Ga ferro-potassic A-type granitoids of southern Norway by extreme
944 differentiation from basic magmas. Precambrian Research 124, 107-148.
945 Wan, Y., Xie, H., Yang, H., Wang, Z., Liu, D., Kroener, A., Wilde, S.A., Geng, Y., Sun, L., Ma, M., 2013a.
946 Is the Ordos block Archean or Paleoproterozoic in age? Implications for the Precambrian evolution
947 of the North China Craton. American Journal of Science 313, 683-711.
948 Wan, Y., Xu, Z., Dong, C., Nutman, A., Ma, M., Xie, H., Liu, S., Liu, D., Wang, H., Cu, H., 2013b.
949 Episodic Paleoproterozoic (~ 2.45,~ 1.95 and~ 1.85 Ga) mafic magmatism and associated high
950 temperature metamorphism in the Daqingshan area, North China Craton: SHRIMP zircon U–Pb
951 dating and whole-rock geochemistry. Precambrian Research 224, 71-93.
952 Wang, C.Y., Sandvol, E., Zhu, L., Lou, H., Yao, Z., Luo, X., 2014. Lateral variation of crustal structure
953 in the Ordos block and surrounding regions, North China, and its tectonic implications. Earth and
954 Planetary Science Letters 387, 198-211.
955 Wang, D., Guo, J., 2017. Late Archean high-pressure pelitic granulites in the Yinshan block, North China
956 Craton. Precambrian Research 303, 251-267.
957 Wang, J., Jia, H., Tao, C., Zhao, Y., Ma, L., Sun, X., Dong, Z., Wang, F., 2023a. Source and enrichment
958 regularity of helium in Dongsheng Gas Field of Hangjinqi area, Ordos Block. Natural Gas
959 Geoscience 34, 566-575.
960 Wang, L., Guo, J., Yin, C., Peng, P., Zhang, J., Spencer, C.J., Qian, J., 2018. High-temperature S-type
961 granitoids (charnockites) in the Jining complex, North China Craton: Restite entrainment and
962 hybridization with mafic magma. Lithos 320-321, 435-453.
963 Wang, L.-J., Guo, J.-H., Yin, C., Peng, P., 2017. Petrogenesis of ca. 1.95 Ga meta-leucogranite
964 s from the Jining Complex in the Khondalite Belt, North China Craton: Water-fluxed melt
965 ing of metasedimentary rocks. Precambrian Research 303, 355-371.
966 Wang, X., Li, X.P., Zhang, J., Schertl, H.P., 2020. Geochemistry, geochronology and evolution of
967 Paleoproterozoic granitoid gneisses in the Khondalite Belt, North China Craton. Precambrian
968 Research 338, 105590.
969 Wang, X., Li, X.-P., Zhang, J., Zhou, H., Yin, C., 2022a. Paleoproterozoic A1- and A2-type coexisting
970 monzogranites in the Daqingshan Complex, Khondalite Belt, North China Craton and its tectonic
971 implications. Precambrian Research 369, 106518.
972 Wang, X., Zhang, J., Liu, Q., Zhou, H., Yin, C., Zhang, S., Chen, Y., Cheng, C., Guo, M., 2023b.
973 Petrogenesis and tectonic setting of Neoarchean tonalitic-trondhjemitic-granodioritic gneisses in the
974 Xiwulanbulang area of the Yinshan block, North China craton. GSA Bulletin 135, 2922-2938.
975 Wang, X., Zhang, J., Yin, C., Liu, X., Chen, Y., Cheng, C., Guo, M., 2022b. Petrogenesis and tectonic
976 implications of 1.86–1.80 Ga A-type granites in the Daqingshan Complex, Khondalite Belt, North
977 China Craton. Precambrian Research 378, 106757.
978 Wang, X., Zhang, J., Yin, C., Qian, J., Gao, P., Zhang, S., Liu, X., Chen, Y., Zhao, C., 2022c. A syn- to
979 post-collisional tectonic transition in the Khondalite Belt, North China Craton: Constraints from
980 1.95 - 1.93 Ga adakitic granitoids in the Daqingshan Complex. Precambrian Research 374, 106648.

Wang, X., Zhang, J., Yin, C., Zhou, H., Liu, J., Liu, X., Zhao, C., 2021. Petrogenesis and tectonic implications of TTG granitoids from the Daqingshan complex of the Khondalite belt, North China craton. American Journal of Science 321, 680-707.

Wang, Y., Li, Z., Pei, X., Wang, M., Zhou, H., Wang, R., Zhang, T., Lin, H., Hussain, I., Wang, X., 2025. Paleoproterozoic continental crust accretion on the northern margin of the North China Craton: Evidence from the Shangyi Complex at the eastern segment of the Khondalite Belt. Precambrian Research 422, 107774.

Whalen, J.B., Currie, K.L., Chappell, B.W., 1987. A-type granites: geochemical characteristics, discrimination and petrogenesis. Contributions to mineralogy and petrology 95, 407-419.

Xu, C., Sun, F., Fan, X., Li, L., Liu, J., Yu, L., 2020. Late Paleoproterozoic crustal evolution in the Daqingshan area: Evidences from adakitic and A-type granitoids in the Guyang Changshengqu goldfield, Khondalite Belt, North China Craton. Precambrian Research 345, 105761.

Xu, C., Sun, F., Fan, X., Li, L., Liu, J., Yu, L., 2020. Late Paleoproterozoic crustal evolution in the Daqingshan area: Evidences from adakitic and A-type granitoids in the Guyang Changshengqu goldfield, Khondalite Belt, North China Craton. Precambrian Research 345, 105761.

Yin, C., Zhao, G., Guo, J., Sun, M., Xia, X., Zhou, X., Liu, C., 2011. U–Pb and Hf isotopic study of zircons of the Helanshan Complex: constrains on the evolution of the Khondalite Belt in the Western Block of the North China Craton. Lithos 122, 25-38.

Yin, C., Zhao, G., Sun, M., Xia, X., Wei, C., Zhou, X., Leung, W., 2009. LA-ICP-MS U–Pb zircon ages of the Qianlishan Complex: constrains on the evolution of the Khondalite Belt in the Western Block of the North China Craton. Precambrian Research 174, 78-94.

Yin, C., Zhao, G., Wei, C., Sun, M., Guo, J., Zhou, X., 2014. Metamorphism and partial melting of high-pressure pelitic granulites from the Qianlishan Complex: constraints on the tectonic evolution of the Khondalite Belt in the North China Craton. Precambrian Research 242, 172-186.

Zhang, C., Diwu, C., Kröner, A., Sun, Y., Luo, J., Li, Q., Gou, L., Lin, H., Wei, X., Zhao, J., 2015. Archean-Paleoproterozoic crustal evolution of the Ordos Block in the North China Craton: Constraints from zircon U–Pb geochronology and Hf isotopes for gneissic granitoids of the basement. Precambrian Research 267, 121-136.

Zhang, C., Gou, L., Bai, H., Hu, Y., Wu, C., 2021. New thinking and understanding for the researches on the basement of Ordos Block. Acta Petrologica Sinica 37, 162-212.

Zhang, H.F., Wang, H.Z., Santosh, M., Zhai, M.G., 2016. Zircon U–Pb ages of Paleoproterozoic mafic granulites from the Huai'an terrane, North China Craton (NCC): Implications for timing of cratonization and crustal evolution history. Precambrian Research 272, 244-263.

Zhang, H.F., Zhai, M.G., Santosh, M., Diwu, C.R., Li, S.R., 2011. Geochronology and petrogenesis of Neoarchean potassic meta-granites from Huai'an Complex: Implications for the evolution of the North China Craton. Gondwana Research 20, 82-105.

Zhang, H.F., Zhai, M.G., Santosh, M., Li, S.R., 2012. Low-Al and high-Al trondhjemites in the Huai'an Complex, North China Craton: Geochemistry, zircon U–Pb and Hf isotopes, and implications for Neoarchean crustal growth and remelting. Journal of Asian Earth Sciences 49, 203-213.

Zhang, J., Wang, D., Guo, J., Ren, Y., Tian, H., Wang, H., Tong, X., Zhang, Y., Shi, J., Chang, Q., Xiang, Z., 2023. Petrogenesis of the ca. 2.5 Ga dioritic-TTG and granitic gneisses from the Huai'an

Complex and its implications for crustal evolution and tectonic settings of the North China Craton. Lithos 444-445, 107-114.

Zhang, L., Liu, C., Fayek, M., Wu, B., Lei, K., Cun, X., Sun, L., 2017. Hydrothermal mineralization in the sandstone–hosted Hangjinqi uranium deposit, North Ordos Block, China. Ore Geology Reviews 80, 103-115.

Zhang, W., Li, Y., Zhao, F., Han, W., Li, Y., Wang, Y., Holland, G., Zhou, Z., 2019. Using noble gases to trace groundwater evolution and assess helium accumulation in Weihe Basin, central China. Geochimica et Cosmochimica Acta 251, 229-246.

Zhang, W., LI, Y., Zhao, F., Zhou, Z., Han, W., Zhou, J., Zhang, Q., 2020. Granite is an Effective Helium Source Rock: Insights from the Helium Generation and Release Characteristics in Granites from the North Qinling Orogen, China. Acta Geologica Sinica - English Edition 94, 114-125.

Zhang, X., Yuan, L., Xue, F., Zhai, M., 2014. Neoarchean metagabbro and charnockite in the Yinshan block, western North China Craton: Petrogenesis and tectonic implications. Precambrian Research 255, 563-582.

Zhao, G., Guo, J., 2012. Precambrian geology of China: preface. Precambrian Research 222, 1-12.

Zhao, G., Sun, M., Wilde, S.A., Sanzhong, L., 2005. Late Archean to Paleoproterozoic evolution of the North China Craton: key issues revisited. Precambrian Research 136, 177-202.